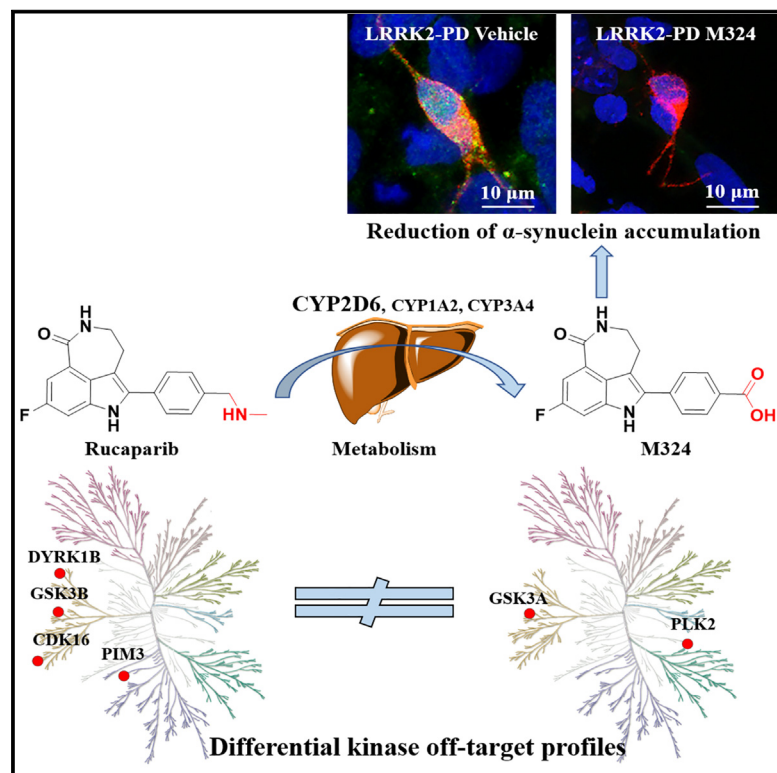


Cell Chemical Biology

Identification of differential biological activity and synergy between the PARP inhibitor rucaparib and its major metabolite

Graphical abstract



Authors

Huabin Hu, Carme Serra, Wenjie Zhang, ..., Miguel Angel Pujana, Amadeu Llebaria, Albert A. Antolin

Correspondence

amadeu.llebaria@iqac.csic.es (A.L.), albert.antolin@icr.ac.uk (A.A.A.)

In brief

Hu et al. comprehensively characterized the kinome profile of the major metabolite of rucaparib, M324. The study uncovers distinct kinase landscapes between rucaparib and M324 that translate into a synergistic effect in prostate cancer cell lines and a unique capacity of M324 to reduce α -synuclein accumulation in iPSC dopamine neurons.

Highlights

- Rucaparib and its major metabolite M324 exhibit differential kinase selectivity
- M324 displays unique PLK2 inhibition at clinically achievable concentrations
- Rucaparib and M324 are synergistic in prostate cancer cell lines
- M324 reduces α -synuclein accumulation in iPSC neurons from Parkinson's patients



Article

Identification of differential biological activity and synergy between the PARP inhibitor rucaparib and its major metabolite

Huabin Hu,¹ Carme Serra,^{2,3} Wenjie Zhang,⁴ Aurora Scrivo,^{5,6} Irene Fernández-Carasa,^{5,6} Antonella Consiglio,^{5,6,7,8} Alvaro Aytes,^{4,8} Miguel Angel Pujana,^{4,8} Amadeu Llebaria,^{2,3,*} and Albert A. Antolin^{1,4,9,*}

¹Center for Cancer Drug Discovery, Division of Cancer Therapeutics, The Institute of Cancer Research, London SM2 5NG, UK

²Medicinal Chemistry and Synthesis (MCS) Laboratory, Institut de Química Avançada de Catalunya (IQAC-CSIC), 08034 Barcelona, Spain

³Synthesis of High Added Value Molecules (SIMChem), Institut de Química Avançada de Catalunya (IQAC-CSIC), 08034 Barcelona, Spain

⁴ProCURE, Catalan Institute of Oncology (ICO), Oncobell, Bellvitge Institute for Biomedical Research (IDIBELL), Barcelona, Catalonia, Spain

⁵Department of Pathology and Experimental Therapeutics, Bellvitge University Hospital-IDIBELL, Hospitalet de Llobregat, Barcelona, Spain

⁶Institute of Biomedicine of the University of Barcelona (IBUB), Barcelona, Spain

⁷Department of Molecular and Translational Medicine, University of Brescia, Brescia, Italy

⁸Senior author

⁹Lead contact

*Correspondence: amadeu.llebaria@iqac.csic.es (A.L.), albert.antolin@icr.ac.uk (A.A.A.)

<https://doi.org/10.1016/j.chembiol.2024.01.007>

SUMMARY

The (poly)pharmacology of drug metabolites is seldom comprehensively characterized in drug discovery. However, some drug metabolites can reach high plasma concentrations and display *in vivo* activity. Here, we use computational and experimental methods to comprehensively characterize the kinase polypharmacology of M324, the major metabolite of the PARP1 inhibitor rucaparib. We demonstrate that M324 displays unique PLK2 inhibition at clinical concentrations. This kinase activity could have implications for the efficacy and safety of rucaparib and therefore warrants further clinical investigation. Importantly, we identify synergy between the drug and the metabolite in prostate cancer models and a complete reduction of α -synuclein accumulation in Parkinson's disease models. These activities could be harnessed in the clinic or open new drug discovery opportunities. The study reported here highlights the importance of characterizing the activity of drug metabolites to comprehensively understand drug response in the clinic and exploit our current drug arsenal in precision medicine.

INTRODUCTION

Small-molecule drugs administered orally are normally metabolized through proteins, such as cytochrome P450 enzymes, that catalyze chemical modifications aimed at increasing aqueous solubility to facilitate excretion.^{1–3} Accordingly, drug metabolites often do not display relevant *in vivo* activity,^{2,3} although certain drug metabolites are present at high plasma concentrations and can be pharmacologically active.² In these cases, the chemical modifications performed on drug metabolites could alter their interaction with human proteins,^{2,4,5} resulting in a distinct biological activity than their parent drug.^{5–7} Unfortunately, drug metabolites are rarely characterized comprehensively in preclinical models, are often not commercially available to facilitate testing, and their wider protein-binding activity is often overlooked. As any other small molecule, drug metabolites can interact with multiple protein targets simultaneously, a behavior termed polypharmacology.^{8–11} Therefore, systematically characterizing the polypharmacology of drug metabolites that are

present at high plasma concentrations could help clarify the unexplained clinical activity of drugs, better tailor drugs to patients, and open new repurposing opportunities.

Poly(ADP-ribose) polymerase-1 (PARP1) inhibitors are an established class of targeted, small-molecule drugs approved for various types of cancers displaying alterations in DNA repair.^{12–14} Four PARP1 inhibitors (olaparib, rucaparib, talazoparib, and niraparib) have been approved by the Food and Drug Administration (FDA),¹⁵ all of them sharing a benzamide substructure that mimics the nicotinamide moiety of PARP1's substrate NAD⁺ to form a hydrogen bond network in the binding site (Figure 1).¹⁶ Given these conserved interactions, FDA-approved PARP inhibitors share a similar profile against PARP enzymes, displaying low selectivity between PARP1-3 and modest activity against other PARPs,^{15,17} and share many side effects.^{15,18,19} However, it has been reported that there are side effects specific to each PARP inhibitor that cannot be explained by their similar selectivity profiles against PARP enzymes.^{15,18}



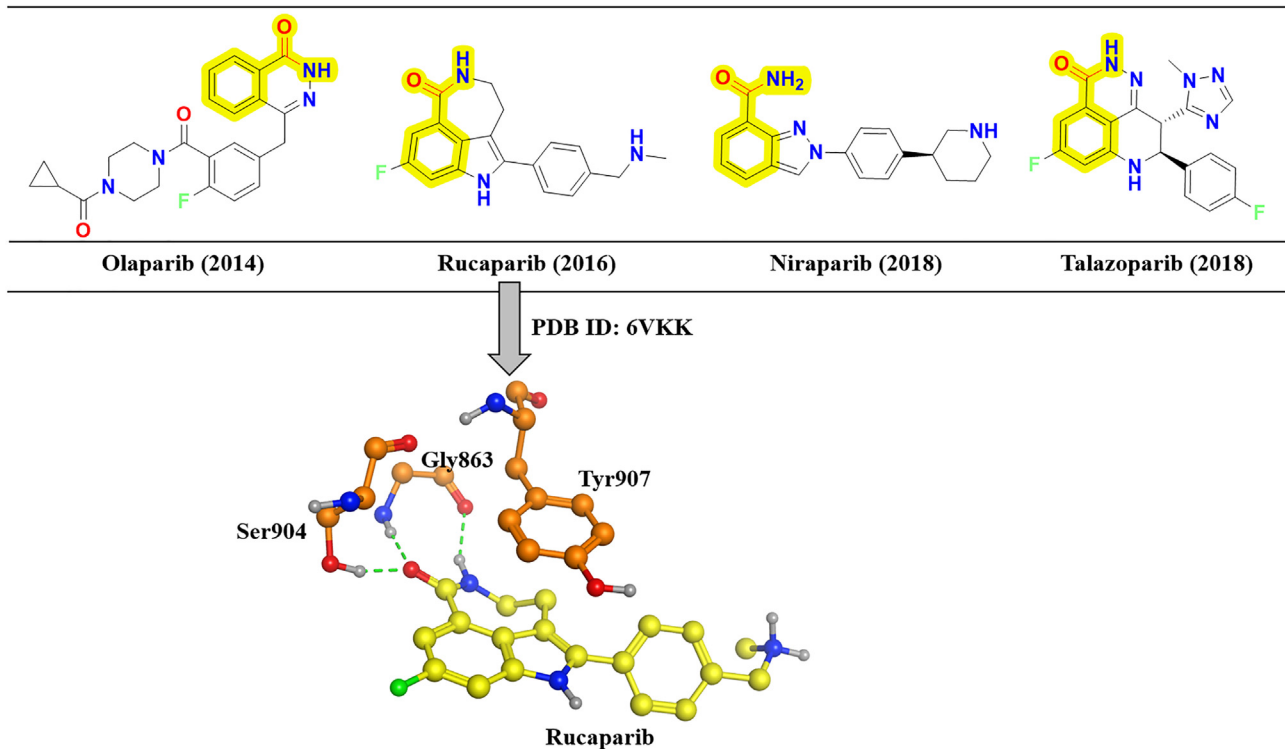


Figure 1. FDA-approved PARP1 inhibitors and key molecular interactions

The chemical structures of the four PARP1 inhibitors approved by the FDA are displayed in the upper panel. The substructure (benzamide) mimicking the nicotinamide moiety of the PARP1 substrate NAD⁺ is highlighted in yellow on each chemical structure. The year of the first FDA approval is shown in brackets. The lower panel exemplifies the key conserved interactions between PARP1 and its inhibitors using rucaparib as an example. For clarity, only key interactions with the core scaffold of rucaparib are depicted. The carbons of key PARP1 residues and rucaparib are colored orange and yellow, respectively.

Despite their conserved interactions, all FDA-approved PARP1 drugs have a unique chemical structure (Figure 1). Our group, alongside others, demonstrated that each approved PARP inhibitor has different polypharmacological profiles across the human kinome.^{15,20} While olaparib and talazoparib are unlikely to modulate kinase activity, niraparib and rucaparib showed significant kinase polypharmacology.¹⁵ Rucaparib exhibited submicromolar *in vitro* activity against DYRK1B, CDK16, and PIM3, whereas niraparib potently inhibited DYRK1A and DYRK1B.¹⁵ These results enabled to link some of the differential side effects observed between PARP inhibitors to their different kinase off-targets. For example, unique PIM3 inhibition by rucaparib could explain the increased cholesterol levels observed in some patients taking this drug, which have not been observed with other PARP inhibitors.¹⁵ However, many differential side effects between PARP inhibitors remain unexplained, including the increased number of cardiac adverse drug reactions only observed in patients taking rucaparib.¹⁹

Rucaparib is metabolized predominantly by CYP2D6 to its major metabolite M324 (a carboxylic acid, Figure 2A) which can be detected in several species, including mouse and human.^{21,22} In animal models, M324 can reach higher concentrations in plasma than the parent drug but with lower concentration inside tumor cells. Still, M324 was able to reach single-digit micromolar concentrations inside tumor cells and was detectable two days after oral administration.²² In humans, M324 is the major detectable metab-

olite in plasma with concentration up to ~40% of rucaparib's concentration.²¹ Although a study reported that M324 showed limited PARP1 inhibition in intact human cells²² and that it was "at least 30-fold less potent than rucaparib against PARP1-3" (https://www.ema.europa.eu/en/documents/product-information/rubraca-par-product-information_en.pdf), the micromolar concentrations that M324 can reach inside mice tumors demonstrate its cellular permeability. Accordingly, its potential pharmacological activity, particularly beyond the PARP enzyme family, warrants further investigation and could help explain the unique clinical activity of rucaparib.

Here, we have comprehensively characterized the kinase off-target profile of M324 using computational approaches followed by experimental validation. Our experimental results confirmed our hypothesis that M324 and its parent drug have differential kinase polypharmacology that could have implications for the clinical efficacy and safety of rucaparib. In particular, we identify synergy between rucaparib and M324 in prostate cancer cell lines that could influence current combinatorial clinical trials of rucaparib in advanced prostate cancer. We also investigated the effects of M324 on the endogenous accumulation of α -synuclein, a major constituent of Lewy bodies, in disease-relevant cell types from patients with Parkinson's disease (PD).²³ Treatment of PD dopamine neurons, differentiated from induced pluripotent stem cells (iPSC) lines obtained from a PD patient carrying the LRRK2 G2019S mutation, was effective in reducing

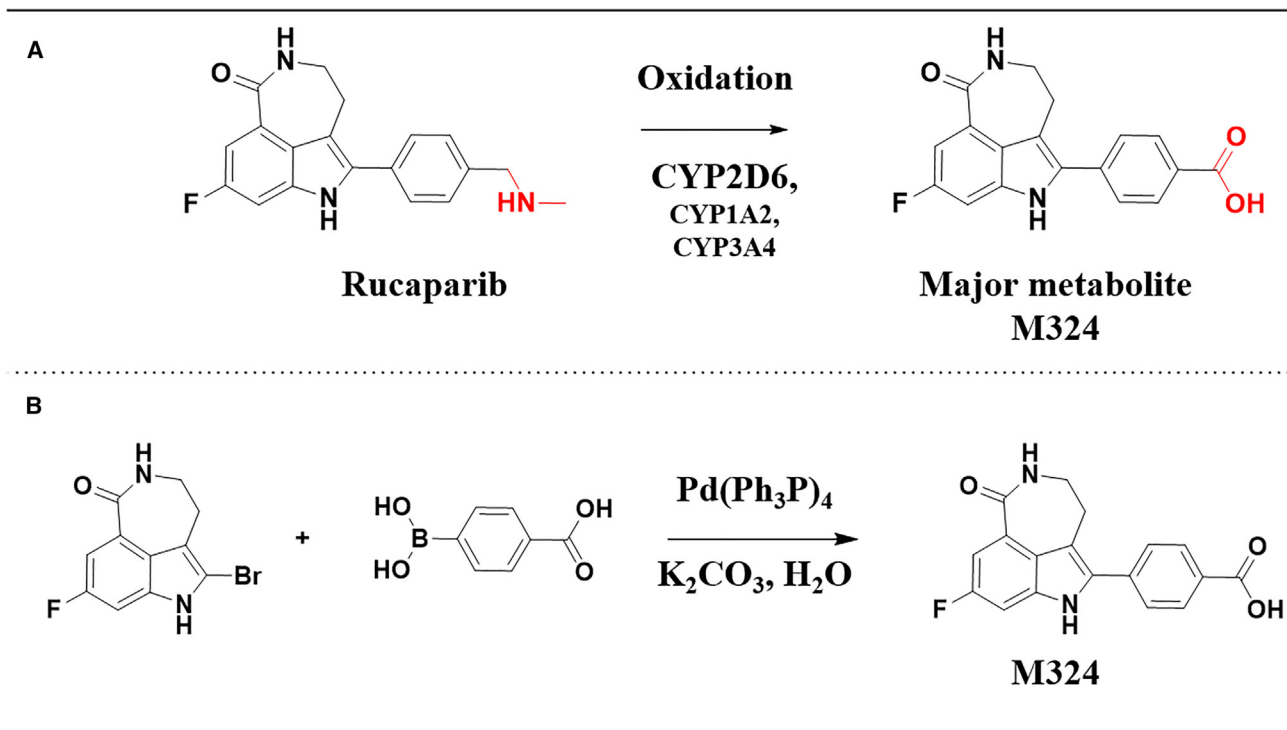


Figure 2. Biotransformation of rucaparib to its main metabolite and corresponding synthesis scheme

(A) Cytochrome P450-mediated oxidative deamination of rucaparib, which yields the major metabolite (M324). The structural modification showing the change from an amine to a carboxylic acid is colored red.

(B) Synthesis of the metabolite M324 using a Suzuki cross-coupling reaction.

the abnormal accumulation of α -synuclein. Thus, our findings in a genuinely human experimental model of PD highlight the therapeutic potential of the metabolite alone and pave the way for the repurposing and drug discovery opportunities in this neurodegenerative disease.

RESULTS

Chemical synthesis of rucaparib's major metabolite M324

Most drugs are readily available for purchase from chemical vendors. Unfortunately, most drug metabolites are absent from vendor catalogs, limiting their experimental study and characterization by the wider scientific community. Accordingly, we first synthesized this metabolite via one-step Suzuki cross-coupling reaction starting with two available reagents (2-bromo-8-fluoro-4,5-dihydro-1H-azepino[5,4,3-cd]indol-6(3H)-one and 4-boronobenzoic acid), as illustrated in Figure 2B. The resulting product was purified and obtained as a greenish solid (71% yield). The chemical structure of the compound has been confirmed by NMR and was $\geq 95\%$ pure by HPLC/MS and the structure of the parent drug which was purchased by a commercial vendor was also confirmed by NMR (Figures S1 and S2).

Computational methods predict different kinase polypharmacology between rucaparib and M324

Several computational methods have been developed for polypharmacology prediction using public bioactivity data.^{24,25} In

this study, we employed four different *in silico* approaches, covering both ligand- and structure-based methods, to predict potential kinase off-targets of rucaparib and M324, namely (1) the six independent ligand-based methods integrated in the CLARITY platform developed by Chemotargets;²⁶ (2) the similarity ensemble approach (SEA),²⁷ a web-based tool to conduct target prediction based on chemical similarity; (3) the polypharmacology browser PPB2 incorporating different models (e.g., fingerprint comparison, machine learning, or deep learning) to predict potential targets for compounds;²⁸ and (4) GalaxySagittarius software which integrates ligand- and structure-based approaches to derive target hypothesis for a query compound.²⁹ The results of the computational methods concerning only human protein kinases (Tables S1–S4) are summarized in Figure 3.

In total, 75 and 56 kinases were predicted to be potential kinase off-targets for rucaparib and its major metabolite, respectively (Figures 3 and 4B). Most of the kinase predictions for both compounds are derived from GalaxySagittarius with 66 kinases predicted for rucaparib and 39 for M324 (Figures 3 and 4B). The agreement between computational methods at predicting kinase off-targets was low. Only 12 kinases were suggested by at least two computational approaches for both rucaparib and M324, as it can be observed in the Venn diagrams in Figure 3. To gain further insights on these predictions, we constructed a network connecting the predicted kinase targets with either rucaparib or M324 (Figure 3). In general, there is no clear and high enrichment in any kinase group among the predictions.

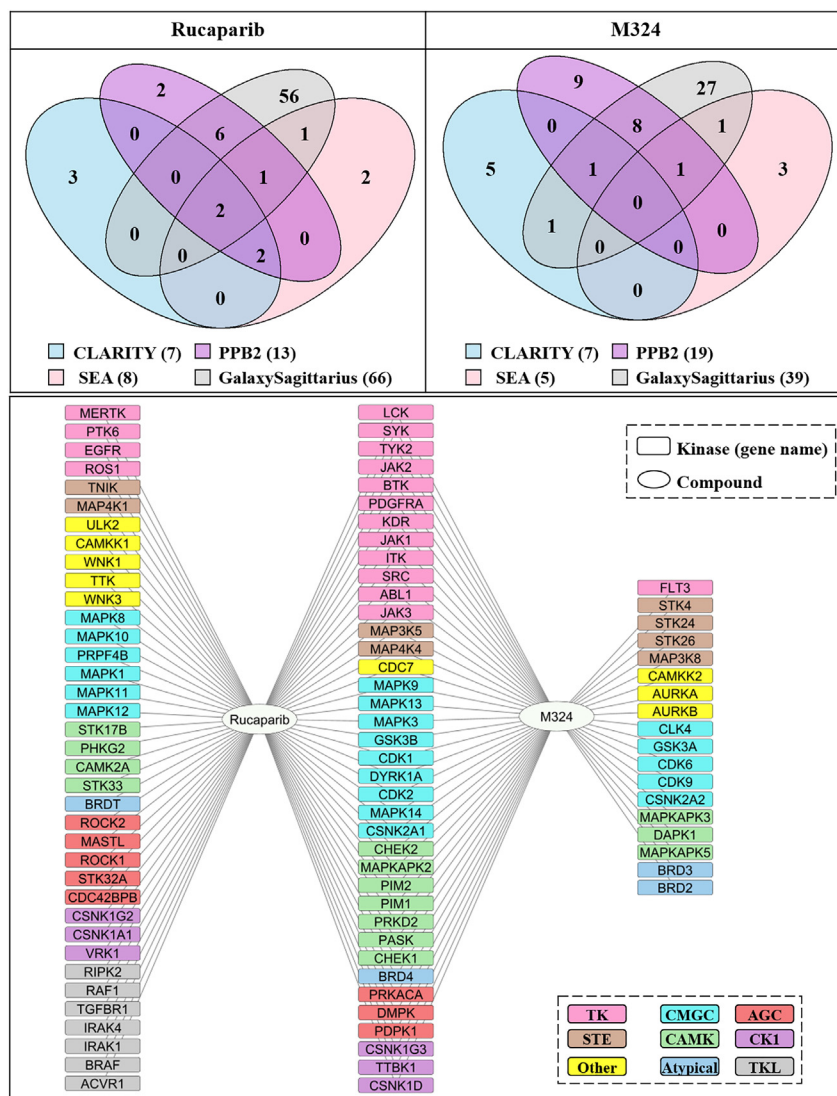


Figure 3. Computationally predicted kinase off-targets of rucaparib and M324 using four different approaches

On top, two Venn diagrams summarize the overlap between the predicted kinases using different computational methods. A detailed overview for the predicted kinases is provided at the bottom network, where rectangle and circular nodes represent kinases and compounds, respectively. The gene name of each kinase is shown inside each rectangular node. Kinase and compound nodes are connected if the kinase is predicted as potential target for the compound through at least one of the computational methods used (see STAR methods). In addition, predicted kinases are colored according to their kinase group annotations implying their structural and functional similarity. In total, rucaparib and M324 are predicted to bind to kinases from nine kinase groups.

(STAR methods). A percentage of inhibition $\geq 50\%$ at $10 \mu\text{M}$ concentration was set as a threshold to consider potential kinase off-targets as hits (Table S5). Using this cutoff, 28 kinases were identified as off-target hits for M324. Figure 4A provides a visual summary of the kinome screening results of M324 across 370 human kinases. Kinase hits are represented by red and green dots. Circle size is proportional to the percentage of inhibition, 100% inhibition corresponding to the largest dots. Kinases inhibited by more than 90% are shown in green and represent the most potent off-targets for M324.

We had previously experimentally characterized the kinome profile of rucaparib at $10 \mu\text{M}$,¹⁵ which allows us to compare the kinome profiles of both compounds. As illustrated in Figure 4A, rucaparib is more promiscuous than its major metabo-

Given the high structural similarity between them, the two compounds have 38 overlapping predicted kinases, most of which belong to TK, CMGC, and CAMK kinase groups. However, there are also many predicted kinases that are not shared: 37 kinases (Figure 3) are exclusively predicted for rucaparib and 18 kinases for M324. Given these results, we hypothesized that M324 could be modulating several unique kinases, different from those inhibited by rucaparib.

Experimental *in vitro* kinome profiling confirms differential polypharmacology between rucaparib and M324

In order to experimentally confirm the computational predictions, we evaluated the activity of the metabolite M324 across the kinome using biochemical experiments on isolated proteins. Specifically, we used Reaction Biology's HotSpot platform (<http://www.reactionbiology.com>) that measures the inhibition of the incorporation of radiolabeled phosphate into the protein substrate to directly obtain the kinase catalytic activity

lite and inhibits 50 kinases across the entire kinome tree. In contrast, M324 has a more limited kinase polypharmacology, inhibiting 28 kinases mainly from the CK1, CAMK, and CMGC groups (Figure 4A). The two compounds only share eight off-target kinases including GSK3A, and M324 tends to be less potent among majority of them. For example, rucaparib showed $\sim 98\%$ inhibition against MYLK4 at $10 \mu\text{M}$, whereas M324 only showed $\sim 70\%$ inhibition. Importantly, M324 strongly inhibited kinases that are not inhibited by rucaparib, such as PLK2, confirming the different kinase polypharmacology between both compounds. A limitation of this analysis is that the two compounds were tested in two different screening platforms but both screening technologies are well validated and regularly used by academia and pharma industry to assess kinase selectivity. Given minor differences in the kinase coverage of the two screening platforms, seven kinase off-targets for rucaparib were not tested for M324, and five kinases that were weakly inhibited by M324 had not been tested for rucaparib, as shown by small white circles on Figure 4A. Therefore, we decided to confirm

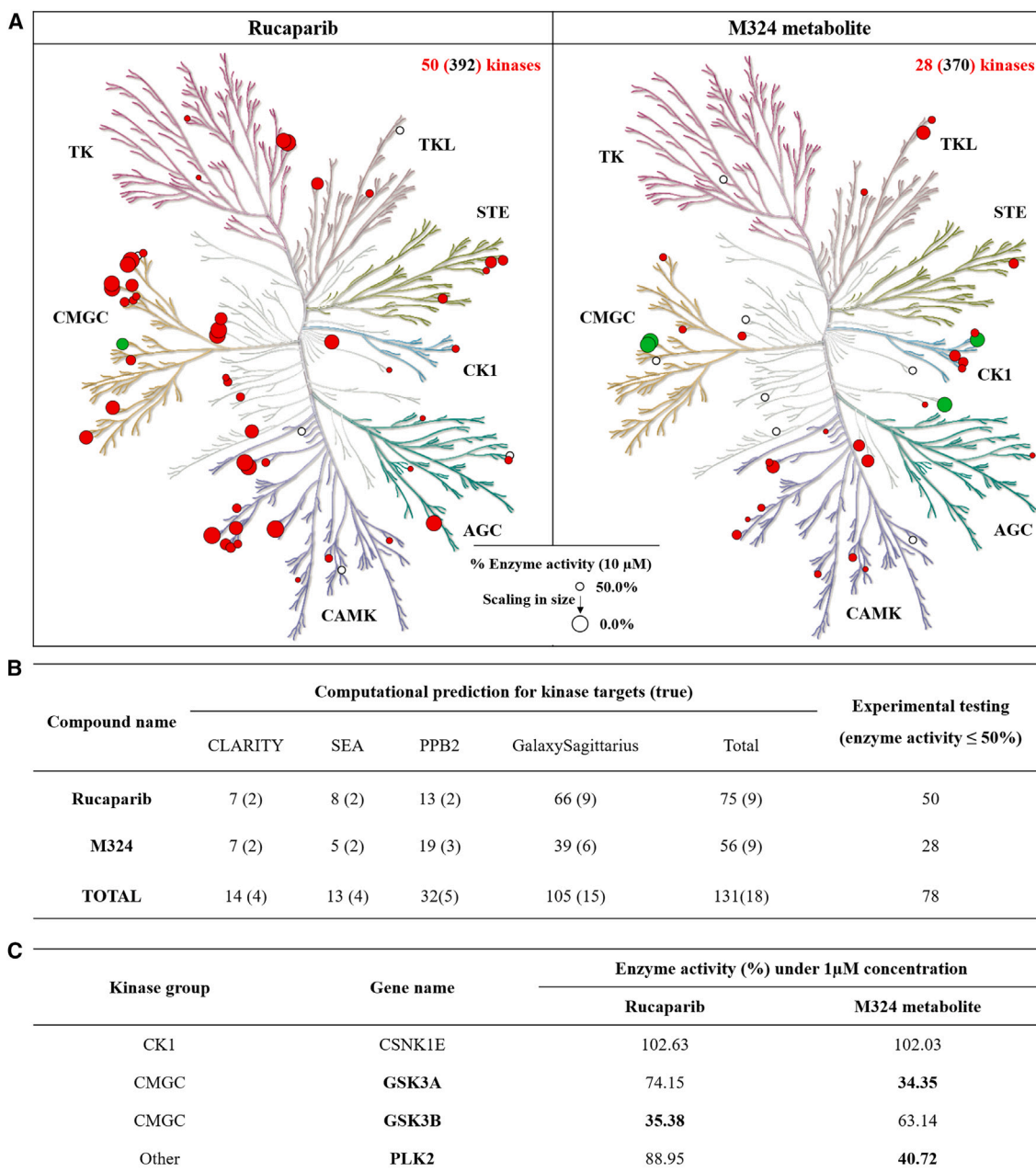


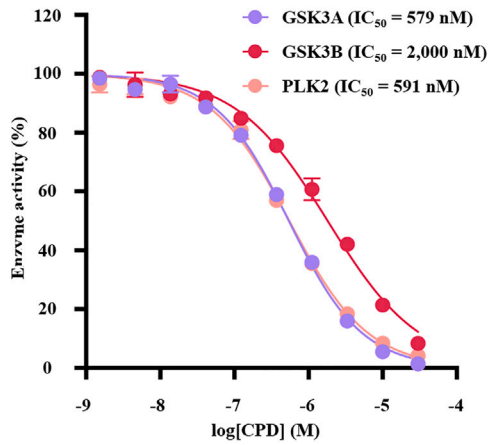
Figure 4. Experimental *in vitro* kinome screening of rucaparib and its major metabolite M324

(A) Kinome trees showing the experimentally confirmed kinase hits at 10 μ M concentration (red and green dots) for rucaparib (data derived from ref. 15) and M324 (data from this work). A threshold of reducing kinase activity below 50% was applied to define a kinase hit. Kinases inhibited by more than 90% by M324 are shown in green. Circle size is proportional to the percentage of inhibition, 100% inhibition being the largest dots. White circles represent kinase hits of M324 that were not tested in rucaparib, or vice versa. Staurosporine was used as a control in most of the assays.

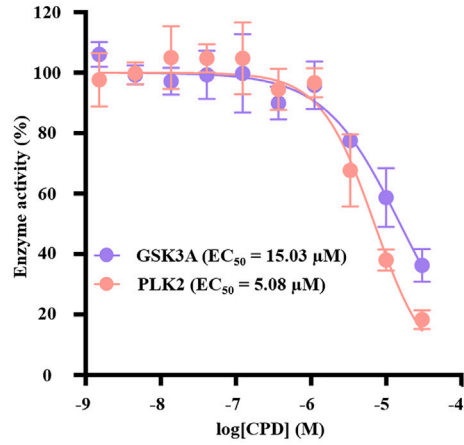
(B) Computational and experimental kinome profiling statistics for rucaparib and M324. The number of kinases predicted using the four different computational methods (see STAR methods) and the number of real kinase hits confirmed by experimental testing (\leq 50% kinase activity at 10 μ M threshold) are shown for both rucaparib and M324. The number in parentheses represents the true predictions confirmed by experimental testing. Rucaparib was predicted and experimentally confirmed to inhibit a higher number of kinases; however, all the computational methods only identified several of the experimental hits and predicted a significant number of false positives. The last row summarizes the predicted and confirmed hits when jointly combined the numbers.

(C) Experimental kinase activity of rucaparib and M324 at 1 μ M. M324 and rucaparib were screened using biochemical assays on isolated proteins at 1 μ M against the top four kinases more strongly inhibited by M324 at 10 μ M (Figure 4A right). The tests were carried out by using a radiometric catalytic inhibition assay from Reaction Biology which directly measures the inhibition of the kinase catalytic activity. The figure displays the average values of two replicate tests. The kinases that more strongly inhibited by either of them are highlighted in bold.

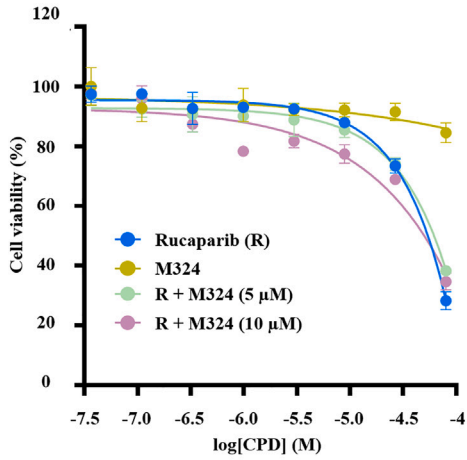
A Isolated protein



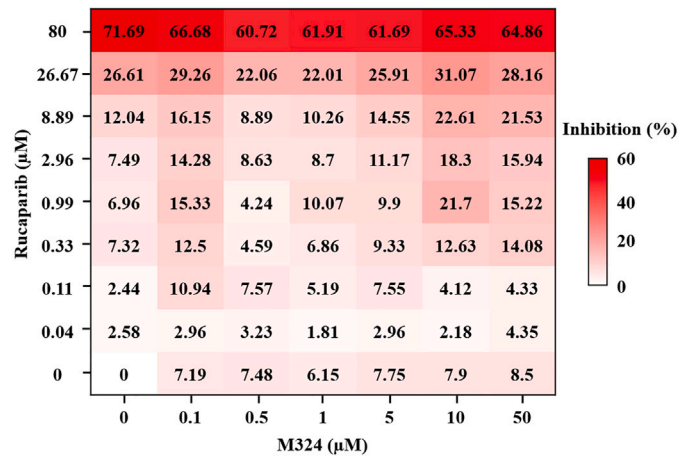
B Intracellular target engagement



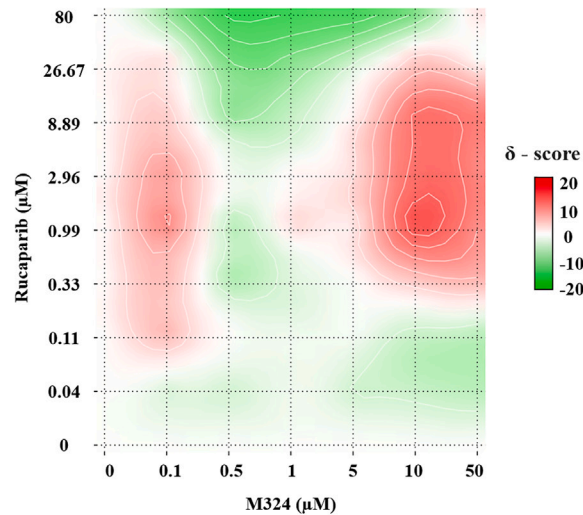
C Combinations



D Dose-response matrix



E Synergy distribution



(legend on next page)

the differences between rucaparib and M324 across a smaller number of kinases using the same platform (see the following experimental section and Figure 4C), which confirmed that each compound has different activities for the selected kinases. Therefore, despite the minor differences between platforms, the large difference on kinase selectivity observed between M324 and rucaparib (Figure 4A) enables us to experimentally confirm our hypothesis that rucaparib and its major metabolite exhibit different kinase polypharmacology.

Having experimentally identified 50 kinase hits for rucaparib and 28 for M324, we can use these data to evaluate the performance of the computational methods used (Figure 4B). If we jointly consider these 78 experimentally validated hits (50 + 28), GalaxySagittarius correctly predicted 15 of them, exhibiting a recall of 19% (15/78) – much better than the 6% (5/78) of PPB2 and the 5% (4/78) of CLARITY and SEA. These values are much lower than the reported recall values of these methods in the literature. For example, PPB2 is reported to have a recall of 81%–76%,²⁸ CLARITY of 48%–80%,²⁶ and GalaxySagittarius of 74%.²⁹ This contrast illustrates the challenges of real-world prospective prediction of new off-targets, where computational methods perform significantly worse than on the retrospective data that is normally used to evaluate them. It must also be stressed that GalaxySagittarius exhibited the best recall but sacrificing precision. GalaxySagittarius correctly guessed 15 of the 105 kinases predicted, which corresponds to a precision of 14% (15/105) – similar to the 15% (5/32) of PPB2 and significantly lower than the 31% (4/13) of SEA and the 29% (4/14) of CLARITY. Overall, if we consider an aggregate of all computational methods used, the recall was 23% (18/78) and the precision was 14% (18/131). These results illustrate the potential of these methods to uncover unknown off-targets of compounds given the thousands of potential targets in the proteome, but also their limited accuracy in predictions as indicated by recall and precision values, highlighting the need for more robust approaches.

Experimental concentration-response experiments demonstrate unique, submicromolar, *in vitro* inhibition of PLK2 and GSK3A by M324

Given the clinical importance of rucaparib for cancer patients, we decided to characterize further the differential kinase polypharmacology between rucaparib and M324. We selected the four kinases potently inhibited by M324 by more than 90% (green circles on the right of Figure 4A)—namely CSNK1E, GSK3A, GSK3B, and PLK2—and tested rucaparib and M324 against them using the same catalytic inhibition assay provided by Reaction Biology (<http://www.reactionbiology.com>) at 1 μ M concentration (Table S6). As shown in Figure 4C, M324 did not inhibit

CSNK1E at 1 μ M concentration (inactive), despite the potent inhibition detected at 10 μ M (Figure 4A). M324 maintained its strong inhibition against GSK3A and PLK2 (< 41% remaining enzyme activity) and inhibited GSK3B, albeit more weakly (63.14% of remaining enzyme activity, Figure 4C). Rucaparib only strongly inhibited GSK3B, showing weak or no activity against the other three targets (Figure 4C). These results further confirmed the different kinase off-target profiles between rucaparib and M324, with the latter showing unique, potent inhibitory effects against GSK3A and PLK2.

For completeness, we also explored the activity of the metabolite across members of the PARP enzyme family (STAR methods). The metabolite shows 100% inhibition for PARP1-2 and TNKS1-2 at 10 μ M concentration, and weaker inhibition for several other PARP family members, a profile that is very similar to that of rucaparib (Tables S7 and S8). This similarity between both profiles across the PARP family prompted us to continue focusing on kinases to identify the main differences between the pharmacology of M324 and rucaparib.

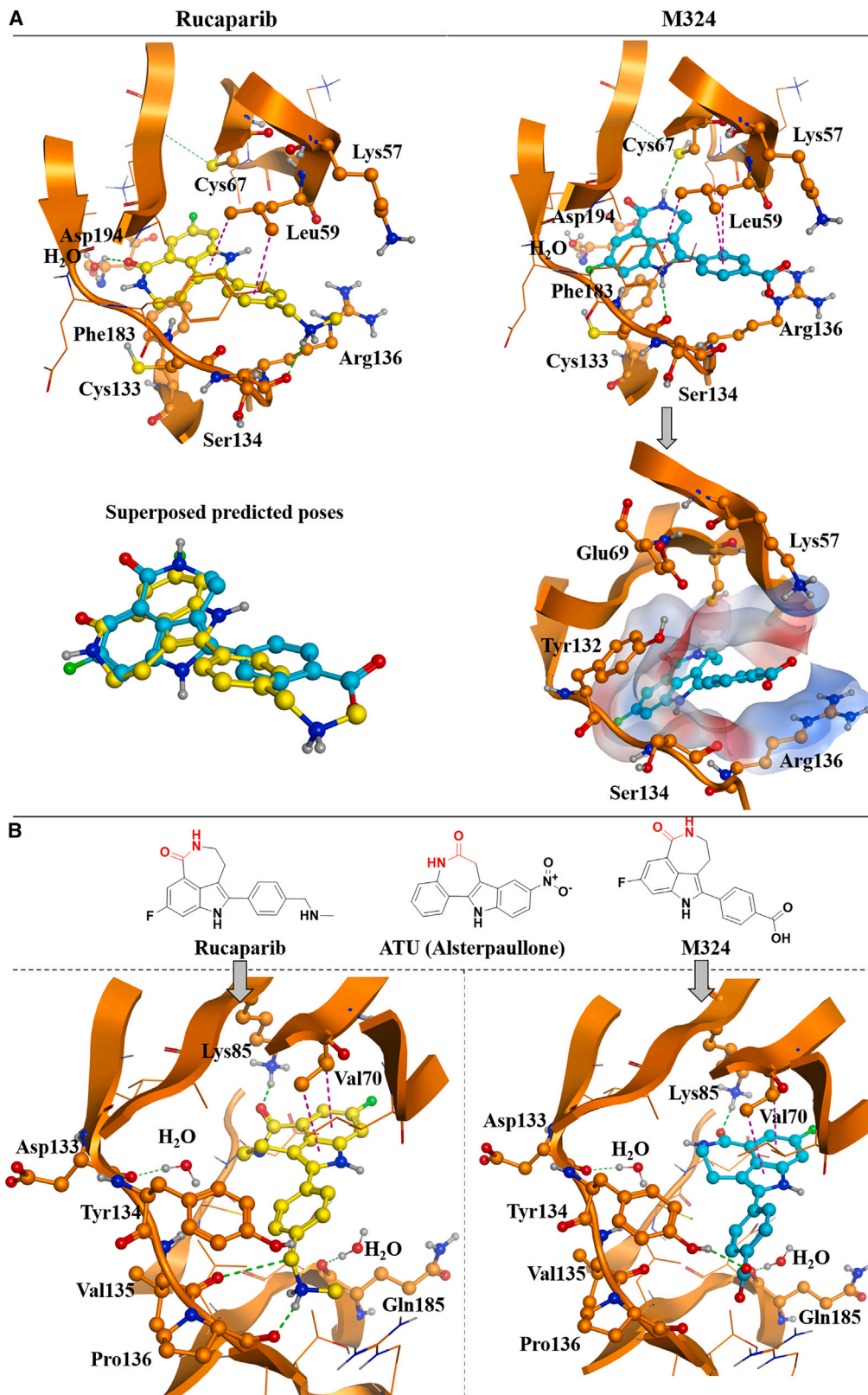
Accordingly, we measured the *in vitro* IC₅₀ values of the three kinase targets (GSK3A, GSK3B, and PLK2) that were potently inhibited by M324 or rucaparib (Figure 4C). As shown in Figure 5A, M324 exhibits strong inhibitory activity against GSK3A (IC₅₀ = 579 nM) and PLK2 (IC₅₀ = 591 nM), and weakly inhibits GSK3B with single-digit micromolar activity (IC₅₀ = 2.0 μ M). Given the reports that M324 can permeate inside cells in animal models and reach micromolar concentrations,²² it was important to explore if these activities on isolated proteins could translate into meaningful intracellular target modulation. We also used an *in silico* web tool (<https://admetmesh.scbdd.com/>) to model cell permeability in Caco-2 cells, and the results suggested that rucaparib and its metabolite have comparable permeability, with predicted values of –5.41 and –5.24 (log unit), respectively.³⁰ Given these results, we decided to perform follow-up intracellular target engagement experiments.

Intracellular target engagement confirms binding of M324 to PLK2 and GSK3A inside HEK293 cells

To determine the kinase activities for M324 inside cells, we used Reaction Biology's Nano-BRET platform (<http://www.reactionbiology.com>) to measure intracellular target engagement for GSK3A and PLK2, the only two kinases potently inhibited by M324 *in vitro* with submicromolar activity (Figure 5A). As shown in Figure 5B, the metabolite shows micromolar activity against PLK2 in HEK293 cells with EC₅₀ value of 5.08 μ M. In contrast, M324 shows weaker cellular activity against GSK3A (EC₅₀ = 15.03 μ M) (STAR methods). Overall, these results

Figure 5. Experimental characterization of the biochemical and intracellular kinase activity of M324 and drug-metabolite combinations

- (A) *In vitro* concentration-response curves and derived IC₅₀ values measured using biochemical assays on isolated proteins in three technical replicates (n = 3) for the three kinases that M324 more potently inhibited are depicted.
- (B) Intracellular target engagement measured using the nanoBRET technology and derived EC₅₀ values of M324 with GSK3A (n = 2) and PLK2 (n = 4). GSK3A was tested in two technical replicates and PLK2 was tested in two independent experiments of two technical replicates to confirm the results (Table S10). Corresponding IC₅₀ and EC₅₀ values are provided. Staurosporine was used as a control in most of the assays.
- (C) Rucaparib and M324 combinations in LNCaP cell line using MTT assay (STAR methods) as a surrogate of cell viability.
- (D) Full dose-response matrix of the combination between rucaparib and M324 in LNCaP.
- (E) Synergy surface plot applying the Bliss model on the combination between rucaparib and M324 in LNCaP. Red indicates positive effect and values of synergy score higher than 10 indicate high-confidence synergy.



(legend on next page)

suggest that PLK2 could be inhibited by M324 inside cells at clinically achievable micromolar concentrations.

In silico molecular docking rationalizes the distinct kinase polypharmacology at the atomic level

To provide a better understanding of the differential kinase off-target profiles between structurally similar rucaparib and M324, the putative binding modes between these two compounds with their kinase off-targets were modeled using the molecular docking method implemented in the MOE software³¹ (see STAR methods for details). Because the crystal structures of GSK3A are yet to be resolved, we focused on PLK2 and GSK3B. First, we analyzed PLK2, which M324 potentially inhibits both *in vitro* and in cells, whereas rucaparib displays very limited kinase activity *in vitro* (around 10% inhibition at 1 μ M concentration, see Figure 4C). As shown in Figure 6A, the predicted binding mode between M324 and PLK2 reveals several favorable interactions: (1) two hydrogen bonds between NHs in the M324 main scaffold and two cysteine residues (Cys67 and hinge residue Cys133) to stabilize the general binding confirmation; (2) the aromatic ring system on which fluorine is attached to form a π - π stacking interaction with residue Phe183; (3) multiple hydrogen- π interactions could be detected which were formed by residue Leu59 with the aromatic ring system of M324; and (4) an electrostatic interaction. Interestingly, the negatively charged terminal carboxylic acid of M324 was favorably sandwiched between the two positively charged residues Lys57 and Arg136, as illustrated in Figure 6A. In contrast, the analysis of interactions between rucaparib and PLK2 uncovers a significantly different pattern. Although a hydrogen bond (with hinge residue Ser134) and two hydrogen- π interactions (with residue Leu59) could be also observed, the positively charged terminal amine group in rucaparib is unfavorably positioned in the environment where two positively charged residues (Lys57 and Arg136) are located—generating a repulsive electrostatic force. Therefore, the different charges of the terminal groups of rucaparib and M324 likely explain the variations of the docking conformations between the two compounds and their significant difference in potency against PLK2 (Figure 6A).

Secondly, we analyzed the putative binding modes for both compounds in GSK3B. Rucaparib exhibits superior GSK3B inhibition (~65% inhibition at 1 μ M concentration), nearly 2-fold stronger than M324 (Figure 4C), albeit both compounds are active. The chemical structures of alsterpauillone, the co-crystallized ligand, and rucaparib (Figure 6B) contain a 7-membered ring with lactam introduced in tricyclic or tetracyclic systems, which greatly contributes to their individual binding behaviors: the lactam in rucaparib interacts with two critical residues Ser904 and

Gly863 in PARP1 (Figure 1), whereas the amide moiety in alsterpauillone forms chelated hydrogen bonds with the hinge residue Val135 in GSK3B (PDB: 1Q3W). However, the different position of the lactam in alsterpauillone and rucaparib implies that rucaparib might adopt a different, less-favorable binding confirmation to better fit into the pocket and interact with the hinge residues of GSK3B. Indeed, the flipped lactam group in M324 and rucaparib results in the loss of Val135-mediated hydrogen bond interaction (Figures 6B), which could explain why both rucaparib and M324 show weaker inhibition against GSK3B in comparison to alsterpauillone. Moreover, the conversion of the secondary amine group to the carboxylic acid in M324 leads to the absence of the hydrogen bonding network with the hinge residues, as depicted in Figure 6B. Instead, the carboxylic acid only forms one hydrogen bond with residue Tyr134, while the rucaparib could still interact with Pro136 which offers a molecular explanation for M324's lower inhibition of GSK3B as compared to its parent drug. Taken together, the docking analysis provides plausible explanations to rationalize the observed differential activity profiles between rucaparib and its main metabolite and helps in the future design of more potent multi-target PARP-kinase inhibitors.

Experimental cancer cell line profiling and combination testing identifies synergy between rucaparib and its major metabolite in prostate cancer lines

After experimentally demonstrating that the metabolite can enter inside transfected human HEK293 cells to engage PLK2 at clinically achievable concentrations and our docking providing a molecular explanation for the unique, potent PLK2 inhibition by M324, it was important to clarify whether the unique polypharmacology of the metabolite could lead to anti-cancer activity in additional, complementary, cancer-relevant models. Accordingly, we experimentally screened rucaparib and M324 across an internal panel of 20 human cancer cell lines using the standard 3-(4,5-dimethylthiazol-2-yl)-2,5-diphenyltetrazolium bromide-based assay (see STAR methods for details), a colorimetric assay measuring cell metabolic activity as a surrogate of cell viability.^{32,33} The cancer cell line panel included lines from several cancer types including prostate, breast, ovarian, pancreatic, and cholangiocarcinoma to cover both the current approved indications of PARP inhibitors and additional cancer types where PARP inhibitors have not been approved (Table S11). Rucaparib showed activity in sixteen cell lines but, unfortunately, the metabolite did not display activity as a single agent in any of the cancer cell lines tested (Table S11)—a result in line with the limited essentiality of PLK2 reported in cancer cell line experiments using CRISPR or RNAi. Next, we decided to test

Figure 6. Computationally predicted binding poses of rucaparib and M324 on PLK2 and GSK3B kinases

(A) The predicted interactions of rucaparib (upper-left panel) and M324 (upper-right panel) on PLK2 kinase (PDB: 4I5M) using the molecular docking environment (MOE) software are shown in the upper panel. Dashed green and magenta lines indicate hydrogen bonds and hydrogen- π interactions, respectively. The superposed predicted binding conformations of M324 and rucaparib are displayed on the bottom left panel. As it can be observed, they adopt distinct conformations, with the amine of rucaparib moving away from the positively charged residues Lys57 and Arg136. The bottom right panel shows the electrostatic surface map around the binding pocket of PLK2 kinase with the binding pose of M324. The surface is colored by electrostatic potential using a continuous spectrum from blue (most positive), through white (neutral) to red (most negative). Two positively charged residues (Lys57 and Arg136) indicate the favorable electrostatic interaction with the negatively charged carboxylic acid moiety of M324.

(B) Predicted binding poses and corresponding interactions of rucaparib (left) and M324 (right) on GSK3B kinase. As it can be observed, neither rucaparib nor M324 is able to mimic the interactions with the hinge region residues Asp133 and Val135 observe with the more potent GSK3B inhibitor co-crystallized, alsterpauillone. Corresponding chemical structures are provided with lactam highlighted in red. The carbons of key residues are colored orange.

a fixed dose, micromolar combination of rucaparib and M324 to explore whether they could be synergistic in any of these 20 cancer cell lines. We found that the single-dose combination had increased inhibition as compared to rucaparib or M324 alone in nine of the tested cell lines, indicating a potentially synergistic effect (Table S11). The biggest difference was observed in the prostate cancer cell line LNCaP with a difference in inhibition exceeding 30%. Interestingly, the list of nine potentially synergistic cancer cell lines included two additional prostate cancer lines: DU145 (~9% higher inhibition in the combination) and 22RV1 (~4%). The rest of cancer types studied had either one or zero cell lines where the drug and the metabolite were potentially synergistic. Accordingly, we decided to focus on these three prostate cancer cell lines to investigate further the potential synergy between rucaparib and its major metabolite.

We performed several independent, concentration-response experiments of rucaparib combined with fixed concentrations of M324 in the three prostate cancer cell lines (Table S12). As it can be observed for LNCaP cell line in Figure 5C, the combination of rucaparib and M324 reduced cell viability more than rucaparib or M324 alone at several concentrations. Interestingly, the maximum effect appeared at clinically achievable concentrations of 1–10 μM of rucaparib and/or the metabolite.³⁴ The behavior was similar in DU145 while for 22RV1 the differences between rucaparib and the combinations were not statistically significant, in line with the lower effect (~4% for 22RV1 instead of 30% for LNCaP or ~9% for DU145) observed in the single concentration experiment (Tables S11 and S12). Figure 5D presents the full dose-response matrix for LNCaP on all the 48 tested combinations (6 concentrations for the metabolite and 8 for rucaparib). Next, we used these dose-response matrices to estimate whether the combination was synergistic using the SynergyFinder web-application version 3.0 (see STAR methods for details). We explored several reference models to more confidently assess whether rucaparib and M324 were synergistic at any of the tested concentrations, including the widely used Bliss and Loewe models.³⁵ Despite the combination was not synergistic in all the tested concentration combinations, all the reference models identified concentrations where the drug and its metabolite were synergistic for both LNCaP and DU145. For example, in the synergy distribution plot in Figure 5E (LNCaP cell line), it can be observed that using the Bliss independent model, rucaparib and M324 are most synergistic at concentrations between 1–9 μM of rucaparib and 5–50 μM of M324 (stronger red areas in the plot). Synergy scores can be interpreted as the average excess response due to drug interactions (i.e., synergy score of 10 corresponds to 10% of response beyond expectation). Despite there is not a single threshold universally accepted to define synergy, synergy score ≥ 10 is often accepted as the threshold from which the interaction between two compounds is likely to be synergistic³⁵). For both prostate cancer cell lines, the most synergistic area of the synergy plots across models was in the low micromolar range and had values exceeding a synergy threshold of 10. Therefore, we confirm that rucaparib and its major drug metabolite are moderately synergistic in LNCaP and DU145 prostate cancer cell lines at low micromolar concentrations compatible with their concentrations in human plasma (Table S12).

M324 reduces α -synuclein accumulation in iPSC-derived dopamine neurons from a patient with PD

Having observed synergy in prostate cancer cell line models but not independent activity, we wondered whether the metabolite could have activity on its own in another cellular context that could open new repurposing or drug discovery opportunities. The best studied target of PLK2 is α -synuclein, which PLK2 phosphorylates at serine 129.³⁶ Accumulation of misfolded α -synuclein is a hallmark of PD and is believed to play an important role in the pathophysiology of the disease.³⁷ Accordingly, PLK2 has been investigated as a target in PD.³⁷ However, whether PLK2 inhibition worsens PD or is protective, and the exact role of its kinase-dependent and kinase-independent activities, are not completely understood.³⁷ Interestingly, GSK3A and GSK3B have also been implicated in PD.³⁸ These biological activities of GSK3s and PLK2 in PD prompted us to test the metabolite in a disease-relevant, well-characterized human iPSC model of PD.^{39,40} Specifically, we used dopamine neurons differentiated from iPSCs derived from patients diagnosed with familial PD carrying the G2019S mutation in the LRRK2 gene. LRRK2 G2019S is the most common LRRK2 mutation and is associated with approximately 4% of familial PD cases and approximately 1% of sporadic PD cases.⁴¹ We studied such neurons generated from one PD patient carrying the LRRK2 G2019S mutation, which reportedly exhibit abnormal accumulation of α -synuclein, and from a healthy donor as control.^{42,43} After 30 days of differentiation, when looking at α -synuclein, we found that approximately 60% of the LRRK2 G2019S dopamine neurons had an abnormal accumulation of the protein compared with approximately 20% of dopamine neurons from healthy individuals (Figures 7A and 7B). Addition of M324 for 24 h reduced the percentage of LRRK2 G2019S dopamine neurons with elevated α -synuclein accumulation (Figures 7A and 7B) (see STAR methods for details). Importantly, this reduction of α -synuclein accumulation was not accompanied by any sign of toxicity, a limitation suffered by many investigational drugs for PD. To further assess this observed difference, we quantified the percentage of DAn that stained positive for α -synuclein, and we confirmed a statistically significant (ANOVA $p < 0.001$) reduction upon treatment with the metabolite equivalent to the negative control (Figure 7B). Overall, we can confirm a remarkable phenotype of the M324 as a single agent that contradicts the current vision of this metabolite as an inactive compound and opens exciting repurposing and drug discovery opportunities in PD.

DISCUSSION

In this study, we systematically characterized the kinome profile of M324, the main metabolite of the PARP1 inhibitor rucaparib, using computational methods coupled with biochemical and cellular experimental validation, and demonstrated that the metabolite has a unique polypharmacology that translates into synergistic effects with its parent drug in prostate cancer cell lines and an anti-Parkinson's phenotype as a single agent.

The polypharmacology of drug metabolites is seldom comprehensively characterized during drug discovery and development. One of the key limitations currently hampering the study of drug metabolites is their lack of commercial availability.

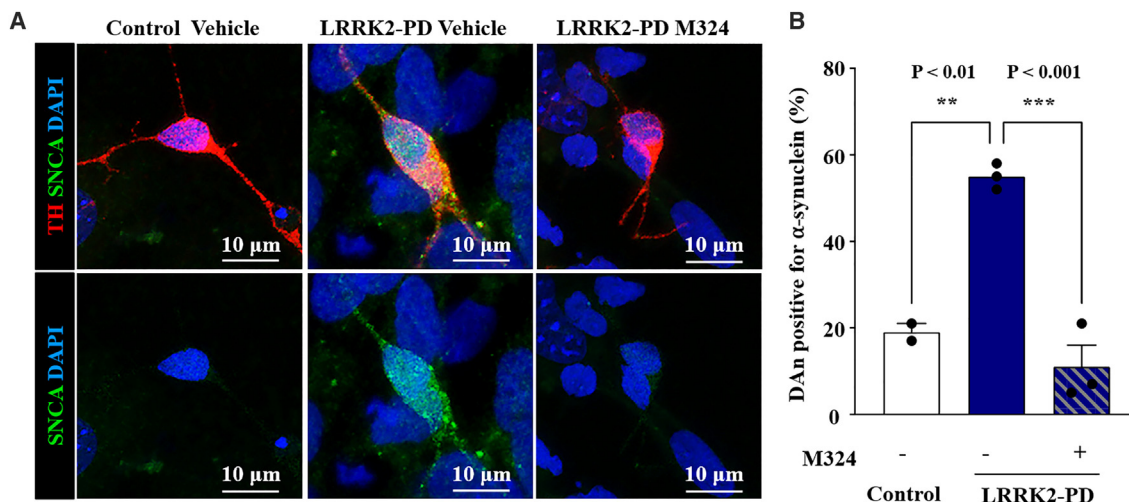


Figure 7. M324 reduces α -synuclein accumulation in hiPSC-derived neurons from a Parkinson's disease (PD) patient

(A) Representative images of dopaminergic neurons (DAN) from control-hiPSC and LRRK2-PD hiPSC co-stained for tyrosine hydroxylase (TH, red – marker of dopaminergic neurons), DAPI (blue – marker of cell nucleus) and α -synuclein (green), treated with M324 (20 μ M). In the upper panel, all the three markers are displayed, while in the bottom panel only α -synuclein and DAPI are displayed to highlight the accumulation of α -synuclein in LRRK2-PD DANs treated with vehicle, and the absence of accumulation in DANs treated with M324 (20 μ M).

(B) Quantitative analyses of DAN positive for α -synuclein. Data are the average of two replicates of one control-hiPSC line, three replicates of one LRRK2-hiPSC line not treated and three replicates of one LRRK2-hiPSC line treated with M324. ANOVA test was used for multiple comparisons. ** $p < 0.01$, *** $p < 0.001$.

Accordingly, we first synthesized the M324 metabolite of rucaparib via one-step Suzuki cross-coupling reaction (Figure 2B). In parallel, we utilized computational approaches to explore potential differences between the polypharmacology of the drug and its metabolite. We had previously used computational methods relying solely on chemical similarity and reported their strengths as well as their limitations in comprehensively identifying polypharmacology.^{15,44} Here, we used four different approaches^{26–29} including GalaxySagittarius, which uses protein structure information alongside chemical information²⁹ and showed the best recall (Figure 4B). We observed a low agreement between different computational methods (Figure 3) that, in addition to the different algorithms employed, could be ascribed to the varying size and target coverage of the databases they use. Therefore, the best recall was achieved when aggregating all the computational methods. Accordingly, we recommend the complementary use of different *in silico* approaches, particularly those using different data sources for training, to maximize the recall. However, the limited precision values of all these methods when used prospectively must be considered carefully before experimental validation while the development of more robust computational approaches remains an unmet need. Overall, *in silico* predictions suggested that M324 could inhibit differential kinases than its parent drug (Figure 3) which had to be confirmed experimentally.

Comprehensive experimental biochemical validation, including enzyme activity measurements at 10 μ M concentration across a large kinase panel (Figure 4A), validation of the most promising results at 1 μ M (Figure 4C), as well as concentration-response curves (Figure 5), confirmed that M324 displayed a unique kinase polypharmacology characterized by strong inhibition of GSK3A and PLK2 ($IC_{50} < 600$ nM) (Figure 5A), none of which are potently inhibited by rucaparib (Figure 4C). This contrasts with the similar

profile of both compounds against PARP enzymes (Tables S7 and S8). Moreover, the inhibition of these two kinases can be effectively translated into cellular activity, with M324 displaying single-digit micromolar binding to PLK2 ($EC_{50} = 5.08$ μ M) in intracellular target engagement assays in transfected HEK293 cells (Figure 5B). Unfortunately, to our knowledge, the free drug concentration of rucaparib or its major metabolite has not been reported.¹⁵ Therefore, it is difficult to draw strong conclusions but given that the reported, steady-state C_{max} concentrations of rucaparib oscillate between 2 and 9 μ M³⁴ and the metabolite reaches 40% of rucaparib's concentration in plasma,²¹ it is possible that M324 could significantly inhibit PLK2 in humans ($EC_{50} = 5.08$ μ M, Figure 5B), which could have implications for the clinical efficacy and safety of rucaparib and therefore warrants further investigation.

Regarding the potential effect of inhibiting PLK2 on human safety, a recent report suggests that the loss of function of PLK2 kinase could induce cardiac fibrosis and promote atrial fibrillation.⁴⁵ We have recently shown that rucaparib has the highest frequency of reported cardiac adverse drug reactions, including arrhythmias¹⁹ – a side effect that has not been reported with olaparib nor with talazoparib. It is tempting to speculate that the unique inhibition of PLK2 by rucaparib's metabolite could be contributing to this higher percentage of reported arrhythmias, although side effects can occur via multiple mechanisms; hence, it would be essential to confirm this hypothesis in clinical trials. If confirmed, these results could further support the use of alternative PARP inhibitors in patients with cardiac illnesses.

Regarding the potential beneficial effects of PLK2 inhibition in oncology, we have shown that M324 and rucaparib exhibit synergy in two prostate cancer cell lines (Figure 5; Table S12). The higher levels of replication stress-induced DNA damage and a dysfunctional S-phase checkpoint observed in PLK2-deficient

cells⁴⁶ provide a mechanistic basis for the observed synergy which could amplify the synthetic lethal interaction between PARP1 and BRCA1/2. Moreover, a signature including upregulation of PLK2 has recently been described in sensitive cell lines after PARP inhibition, which provides an additional link between these two targets.⁴⁷ Albeit the observed synergy was modest, there are currently several trials testing rucaparib and other PARP inhibitors in advanced prostate cancer in combination with other agents such as enzalutamide.⁴⁸ Therefore, the potential synergistic effects of M324 should be explored and clarified on these trials as the combination of rucaparib and its major metabolite could be advantageous over other PARP inhibitors in this setting. In addition, specific patients with altered metabolism could display different responses depending on the amount of M324 in their plasma, thus offering opportunities for the personalized prescription of rucaparib over other PARP inhibitors.

Beyond oncology, PLK2 has been associated to several other diseases including PD.³⁷ Although PLK2 being a target or anti-target in PD remains controversial,³⁷ GSK3A/B are also potential therapeutic targets in this disease,³⁸ which prompted us to test the metabolite in a PD model. We have shown that the metabolite alone is able to reduce α -synuclein accumulation in iPSC-derived dopaminergic neurons from a PD patient without any signs of toxicity (Figure 7). Therefore, there is no doubt that, contrary to the current assumption, the metabolite is pharmacologically active and could potentially be repurposed for PD as a single agent. However, this repurposing opportunity must be thoroughly investigated and validated, in particular to clarify which are the key target(s) involved in this phenotype, whether the metabolite can cross the blood-brain barrier, and whether the micromolar concentrations that we used can be achieved in animal models and humans for longer time periods with similar efficacy and lack of toxicity. It is important to also stress that PARP1 has recently emerged as a potential target in PD.⁴⁹ Overall, the M324 metabolite opens a new route to target the high unmet medical need posed by Parkinson's disease.

Drugs often bind to more than one target⁵⁰ and there is a growing interest in rationally designing multi-target inhibitors that are more efficacious at treating complex diseases.⁵¹ This strategy is rooted in the pioneering development of dual acetylcholinesterase and muscarinic M2 receptor inhibitors for Alzheimer's disease,⁵² the first example of a rationally designed multitarget compound. Since then, multi-target drug design has been explored to target other neurodegenerative disorders,^{52–54} cancer,⁵⁵ and several other diseases.⁵⁶ However, the rational design of compounds active against several targets remains challenging, particularly in the absence of known multi-target starting points,⁴⁴ and therefore is not yet routinely explored in drug discovery campaigns.^{57–59} Several studies have reported the design of inhibitors targeting PARP1 and other cancer-related targets (e.g., BRD4, PI3K, EZH2, and HDACs), but none of them explored GSK3B or PLK2.⁵⁷ It was recently shown that there is a strong synergistic effect between PARP1 and GSK3B inhibition through drug combination studies in colorectal cancer models.⁶⁰ Our previous¹⁵ and current analyses suggest that rucaparib is the only approved PARP1 inhibitor exhibiting sub-micromolar inhibitory activity

against GSK3B (65% of GSK3B inhibition at 1 μ M concentration, Figure 4C). Therefore, rucaparib represents a promising starting point for structural optimization to develop potent dual GSK3B-PARP inhibitors. Furthermore, M324's polypharmacology could serve as a starting point for the rational design of more potent, brain-penetrant dual inhibitors targeting PARP1-PLK2 or triple PARP1-PLK2-GSK3, aiming to modulate potential PD targets. Therefore, our work also unlocks new multi-target drug discovery opportunities. Overall, we demonstrate that drug metabolites can have a different polypharmacology than their parent drugs, highlighting the importance of making drug metabolites commercially available, incorporating them in preclinical studies, and characterizing them more thoroughly during drug discovery and development to comprehensively understand the effects of drugs in the clinic and better tailor drugs to patients in precision medicine.

Limitations of the study

The major limitation of the present study is the focus on kinases. Our computational analysis also predicted several non-kinase targets (e.g., PPARA or PPARG, which stand out due to the prevalence of reported ligands featuring carboxylic acid functional groups found also in M324). Unfortunately, due to limited time and resources and our previous work identifying kinase off-targets of rucaparib, we decided to focus our experimental validation efforts on the kinome. However, given the clinical significance of rucaparib, in the future, it would be important to wider the off-target validation to explore their potential effects in the clinical efficacy and safety of rucaparib. Moreover, we experimentally validated only the most potent kinases at 10 μ M concentration. It is well known that single concentration experiments are not devoid of error that can lead to deprioritizing potent kinases and current kinome panels do not yet comprehensively cover the kinome, so it is possible that we have missed more potent off-target kinases.

SIGNIFICANCE

The comprehensive (poly)pharmacological characterization of major drug metabolites is often overlooked during drug discovery and development, with only the activity against the known primary target being routinely tested alongside phenotypic safety assays mandated by regulatory agencies. However, the chemical modifications that drug metabolites undergo can alter their capacity to interact with human proteins and some metabolites reach sufficient concentrations in human plasma to exert relevant *in vivo* activities. Here, we use computational and experimental methods to comprehensively study the kinase polypharmacology of M324, the major metabolite of the FDA-approved PARP inhibitor rucaparib. We show that M324 displays a distinct kinase polypharmacology profile compared to its parent drug, characterized by strong *in vitro* inhibition of GSK3A and PLK2. We also demonstrate that M324 engages PLK2 inside cells at clinically achievable, single-digit micromolar concentrations and, therefore, could have an influence in the safety and efficacy of rucaparib that warrants further clinical investigation. In particular, the inhibition of PLK2 by M324 could help explain the increased

cardiac adverse drug reactions, including arrhythmias, observed in patients taking rucaparib, due to the known effects of PLK2 inhibition on promoting cardiac fibrosis. Rucaparib and M324 also have synergistic effects in prostate cancer cell lines that warrant further clinical investigation to clarify whether some patients might benefit more from rucaparib than from other PARP inhibitors. Moreover, our results also open the door to the repurposing of M324 in Parkinson and the design of more potent, multi-target PARP1-kinase inhibitors to tackle the high unmet medical need posed by this untreatable neurodegenerative disease. The results reported here may also open a new conceptual perspective in pharmacology that considers drug metabolism not as an undesirable process to degrade and eliminate the true therapeutic molecule from the organism but as a potential advantage. When a drug is given as a monotherapy, the clinical observations are a result of the combined effect of the drug and its metabolites that are unavoidably present *in vivo* and may produce independent, synergistic, or antagonistic effects. Our results support the optimization of metabolites during drug discovery and development as their activities can be relevant in the clinic. Overall, we recommend making drug metabolites more easily available to the scientific community and characterizing them more thoroughly to make the most of them in personalized and precision medicine for the ultimate benefit of patients worldwide.

STAR★METHODS

Detailed methods are provided in the online version of this paper and include the following:

- KEY RESOURCES TABLE
- RESOURCE AVAILABILITY
 - Lead contact
 - Materials availability
 - Data and code availability
- EXPERIMENTAL MODEL AND STUDY PARTICIPANT DETAILS
 - Cell lines
- METHOD DETAILS
 - Procedure for the preparation of metabolite M324
 - Kinase off-target predictions using four different computational methods
 - *In vitro* kinome profiling using biochemical assays on isolated proteins and concentration-response curves
 - *In vitro* PARP family profiling using biochemical assays on isolated proteins
 - Intracellular target engagement kinase assays
 - Docking studies
 - MTT cell viability assays
 - Cell culture experiments with human iPSC lines and M324 treatment
 - Immunofluorescence analyses of iPSC-derived DA neurons
- QUANTIFICATION AND STATISTICAL ANALYSIS
 - IC₅₀, EC₅₀ and hill slope determination
 - Synergy analysis

SUPPLEMENTAL INFORMATION

Supplemental information can be found online at <https://doi.org/10.1016/j.chembiol.2024.01.007>.

ACKNOWLEDGMENTS

A.A.A. received the support of a fellowship from 'la Caixa' Foundation (LCF/BQ/PI22/11910016) and is now an ISCIII-Miguel Servet Fellow supported by the Instituto de Salud Carlos III grant CP23/00115. A.A.A. and H.H. were formerly supported by a Fellowship from The Institute of Cancer Research. C.S. and A.L. thank CSIC (201980E011) and Catalan Government (2017SGR 1604) for their support. This study was also supported by the Spanish Ministry of Science and Innovation (PID2019-108792GB-I00 supported by MCIN/AEI/10.13039/501100011033 and PDC2021-121051-I00) and the ERC-2020-PoC, the Marató de TV3 Foundation (202012-32) to A.C. A.A. is a ISCIII-Miguel Servet Fellow supported by the Instituto de Salud Carlos III grants CPII20/00024 and PI19/00342 and Generalitat de Catalunya – AGAUR grants 2017SGR448 and SGR AGAUR 2021-184. M.A.P. received support from the Instituto de Salud Carlos III grant FIS PI21/01306. A.S. is a fellow granted by the Program Maria Zambrano from the University of Barcelona. A.C. is a recipient of an ICREA "Academia" Award (Generalitat de Catalunya). This work was also supported by the CERCA Program/Generalitat de Catalunya to IDIBELL and FEDER funds/European Regional Development Fund (ERDF) – a way to Build Europe. The authors thank many colleagues and collaborators for helpful discussions and valuable input into the preparation of this manuscript.

AUTHOR CONTRIBUTIONS

A.A.A., H.H., C.S., A.S., A.C., M.A.P., A.A., and A.L. designed the research. H.H. and A.A.A. performed the computational research and managed the *in vitro* kinase testing work. C.S. and A.L. designed and performed the chemical synthesis. W.Z., M.A.P., and A.A. designed and performed all the cancer cell line and synergy experiments. A.S., I.F.-C., and A.C. performed the experiments with the iPSC-derived neurons. A.A.A., H.H., C.S., A.S., I.F.-C., A.C., M.A.P., A.A., and A.L. conducted data analysis and interpretation. A.A.A. and H.H. wrote the manuscript with contributions from all authors.

DECLARATION OF INTERESTS

A.A.A. and H.H. are/were employees of the Institute of Cancer Research (ICR), which has a commercial interest in a range of drug targets, including PARP and protein kinases. The ICR operates a Rewards to Inventors scheme whereby employees of the ICR may receive financial benefit following commercial licensing of a project. A.A.A. has been instrumental in the creation/development of canSAR, the Chemical Probes Portal, and Probe Miner. A.A.A. is/was a consultant of DarwinHealth, Inc.

Received: November 21, 2022

Revised: August 16, 2023

Accepted: January 18, 2024

Published: February 8, 2024

REFERENCES

1. Guengerich, F.P. (2001). Common and uncommon cytochrome P450 reactions related to metabolism and chemical toxicity. *Chem. Res. Toxicol.* *14*, 611–650. <https://doi.org/10.1021/tx0002583>.
2. Fura, A. (2006). Role of pharmacologically active metabolites in drug discovery and development. *Drug Discov. Today* *11*, 133–142. [https://doi.org/10.1016/S1359-6446\(05\)03681-0](https://doi.org/10.1016/S1359-6446(05)03681-0).
3. Zhang, Z., and Tang, W. (2018). Drug metabolism in drug discovery and development. *Acta Pharm. Sin. B* *8*, 721–732. <https://doi.org/10.1016/j.apsb.2018.04.003>.
4. Walther, R., Rautio, J., and Zelikin, A.N. (2017). Prodrugs in medicinal chemistry and enzyme prodrug therapies. *Adv. Drug Deliv. Rev.* *118*, 65–77. <https://doi.org/10.1016/j.addr.2017.06.013>.

5. Thompson, R.A., Isin, E.M., Ogese, M.O., Mettetal, J.T., and Williams, D.P. (2016). Reactive metabolites: current and emerging risk and hazard assessments. *Chem. Res. Toxicol.* **29**, 505–533. <https://doi.org/10.1021/acs.chemrestox.5b00410>.
6. Baillie, T.A., and Rettie, A.E. (2011). Role of biotransformation in drug-induced toxicity: influence of intra- and inter-species differences in drug metabolism. *Drug Metabol. Pharmacokinet.* **26**, 15–29. <https://doi.org/10.2133/dmpk.dmpk-10-rv-089>.
7. Bender, R.P., Lindsey, R.H., Jr., Burden, D.A., and Osheroff, N. (2004). N-acetyl-p-benzoquinone imine, the toxic metabolite of acetaminophen, is a topoisomerase II poison. *Biochemistry* **43**, 3731–3739. <https://doi.org/10.1021/bi036107r>.
8. Anighoro, A., Bajorath, J., and Rastelli, G. (2014). Polypharmacology: challenges and opportunities in drug discovery. *J. Med. Chem.* **57**, 7874–7887. <https://doi.org/10.1021/jm5006463>.
9. Kabir, A., and Muth, A. (2022). Polypharmacology: the science of multi-targeting molecules. *Pharmacol. Res.* **176**, 106055. <https://doi.org/10.1016/j.phrs.2021.106055>.
10. Hopkins, A.L. (2008). Network pharmacology: the next paradigm in drug discovery. *Nat. Chem. Biol.* **4**, 682–690. <https://doi.org/10.1038/nchembio.118>.
11. Bolognesi, M.L. (2019). Harnessing polypharmacology with medicinal chemistry. *ACS Med. Chem. Lett.* **10**, 273–275. <https://doi.org/10.1021/acsmchemlett.9b00039>.
12. Mateo, J., Lord, C.J., Serra, V., Tutt, A., Balmaña, J., Castroviejo-Bermejo, M., Cruz, C., Oaknin, A., Kaye, S.B., and de Bono, J.S. (2019). A decade of clinical development of PARP inhibitors in perspective. *Ann. Oncol.* **30**, 1437–1447. <https://doi.org/10.1093/annonc/mdz192>.
13. Rose, M., Burgess, J.T., O'Byrne, K., Richard, D.J., and Bolderson, E. (2020). PARP inhibitors: clinical relevance, mechanisms of action and tumor resistance. *Front. Cell Dev. Biol.* **8**, 564601. <https://doi.org/10.3389/fcell.2020.564601>.
14. Sinha, S., Molla, S., and Kundu, C.N. (2021). PARP1-modulated chromatin remodeling is a new target for cancer treatment. *Med. Oncol.* **38**, 118. <https://doi.org/10.1007/s12032-021-01570-2>.
15. Antolin, A.A., Ameratunga, M., Banerji, U., Clarke, P.A., Workman, P., and Al-Lazikani, B. (2020). The kinase polypharmacology landscape of clinical PARP inhibitors. *Sci. Rep.* **10**, 2585. <https://doi.org/10.1038/s41598-020-59074-4>.
16. Ferraris, D.V. (2010). Evolution of poly(ADP-ribose) polymerase-1 (PARP-1) inhibitors. From concept to clinic. *J. Med. Chem.* **53**, 4561–4584. <https://doi.org/10.1021/jm100012m>.
17. Thorsell, A.G., Ekblad, T., Karlberg, T., Löw, M., Pinto, A.F., Tréaugues, L., Moche, M., Cohen, M.S., and Schüler, H. (2017). Structural basis for potency and promiscuity in poly(ADP-ribose) polymerase (PARP) and tankyrase inhibitors. *J. Med. Chem.* **60**, 1262–1271. <https://doi.org/10.1021/acs.jmedchem.6b00990>.
18. LaFargue, C.J., Dal Molin, G.Z., Sood, A.K., and Coleman, R.L. (2019). Exploring and comparing adverse events between PARP inhibitors. *Lancet Oncol.* **20**, e15–e28. [https://doi.org/10.1016/S1470-2045\(18\)30786-1](https://doi.org/10.1016/S1470-2045(18)30786-1).
19. Sandhu, D., Antolin, A.A., Cox, A.R., and Jones, A.M. (2022). Identification of different side effects between PARP inhibitors and their polypharmacological multi-target rationale. *Br. J. Clin. Pharmacol.* **88**, 742–752. <https://doi.org/10.1111/bcp.15015>.
20. Knezevic, C.E., Wright, G., Rix, L.L.R., Kim, W., Kuenzi, B.M., Luo, Y., Watters, J.M., Koomen, J.M., Haura, E.B., Monteiro, A.N., et al. (2016). Proteome-wide profiling of clinical PARP inhibitors reveals compound-specific secondary targets. *Cell Chem. Biol.* **23**, 1490–1503. <https://doi.org/10.1016/j.chembiol.2016.10.011>.
21. Liao, M., Watkins, S., Nash, E., Isaacson, J., Etter, J., Beltman, J., Fan, R., Shen, L., Mutlib, A., Kemeny, V., et al. (2020). Evaluation of absorption, distribution, metabolism, and excretion of [(14)C]-rucaparib, a poly(ADP-ribose) polymerase inhibitor, in patients with advanced solid tumors. *Invest. N. Drugs* **38**, 765–775. <https://doi.org/10.1007/s10637-019-00815-2>.
22. Murray, J., Thomas, H., Berry, P., Kyle, S., Patterson, M., Jones, C., Los, G., Hostomsky, Z., Plummer, E.R., Boddy, A.V., and Curtin, N.J. (2014). Tumour cell retention of rucaparib, sustained PARP inhibition and efficacy of weekly as well as daily schedules. *Br. J. Cancer* **110**, 1977–1984. <https://doi.org/10.1038/bjc.2014.91>.
23. Spillantini, M.G., Crowther, R.A., Jakes, R., Hasegawa, M., and Goedert, M. (1998). alpha-Synuclein in filamentous inclusions of Lewy bodies from Parkinson's disease and dementia with lewy bodies. *Proc. Natl. Acad. Sci. USA* **95**, 6469–6473. <https://doi.org/10.1073/pnas.95.11.6469>.
24. Cereto-Massagué, A., Ojeda, M.J., Valls, C., Mulero, M., Pujadas, G., and Garcia-Valve, S. (2015). Tools for in silico target fishing. *Methods* **71**, 98–103. <https://doi.org/10.1016/j.ymeth.2014.09.006>.
25. Lavecchia, A., and Cerchia, C. (2016). In silico methods to address poly-pharmacology: current status, applications and future perspectives. *Drug Discov. Today* **21**, 288–298. <https://doi.org/10.1016/j.drudis.2015.12.007>.
26. Vidal, D., Garcia-Serna, R., and Mestres, J. (2011). Ligand-based approaches to in silico pharmacology. *Methods Mol. Biol.* **672**, 489–502. https://doi.org/10.1007/978-1-60761-839-3_19.
27. Lounkine, E., Keiser, M.J., Whitebread, S., Mikhailov, D., Hamon, J., Jenkins, J.L., Lavan, P., Weber, E., Doak, A.K., Côté, S., et al. (2012). Large-scale prediction and testing of drug activity on side-effect targets. *Nature* **486**, 361–367. <https://doi.org/10.1038/nature11159>.
28. Awale, M., and Reymond, J.L. (2019). Polypharmacology browser PPB2: target prediction combining nearest neighbors with machine learning. *J. Chem. Inf. Model.* **59**, 10–17. <https://doi.org/10.1021/acs.jcim.8b00524>.
29. Yang, J., Kwon, S., Bae, S.H., Park, K.M., Yoon, C., Lee, J.H., and Seok, C. (2020). GalaxySagittarius: structure- and similarity-based prediction of protein targets for druglike compounds. *J. Chem. Inf. Model.* **60**, 3246–3254. <https://doi.org/10.1021/acs.jcim.0c00104>.
30. Xiong, G., Wu, Z., Yi, J., Fu, L., Yang, Z., Hsieh, C., Yin, M., Zeng, X., Wu, C., Lu, A., et al. (2021). ADMETlab 2.0: an integrated online platform for accurate and comprehensive predictions of ADMET properties. *Nucleic Acids Res.* **49**, W5–W14. <https://doi.org/10.1093/nar/gkab255>.
31. Vilar, S., Cozza, G., and Moro, S. (2008). Medicinal chemistry and the molecular operating environment (MOE): application of QSAR and molecular docking to drug discovery. *Curr. Top. Med. Chem.* **8**, 1555–1572. <https://doi.org/10.2174/156802608786786624>.
32. Alegre-Martí, A., Jiménez-Panizo, A., Martínez-Tébar, A., Poulard, C., Peraita-Moreno, M.N., Abella, M., Antón, R., Chifias, M., Eckhard, U., Piulats, J.M., et al. (2023). A hotspot for posttranslational modifications on the androgen receptor dimer interface drives pathology and anti-androgen resistance. *Sci. Adv.* **9**, eade2175. <https://doi.org/10.1126/sciadv.ade2175>.
33. Aguilar, H., Urruticoechea, A., Halonen, P., Kiyotani, K., Mushiroya, T., Barril, X., Serra-Musach, J., Islam, A., Caizzi, L., Di Croce, L., et al. (2014). VAV3 mediates resistance to breast cancer endocrine therapy. *Breast Cancer Res.* **16**, R53. <https://doi.org/10.1186/bcr3664>.
34. McCrudden, C.M., O'Rourke, M.G., Cherry, K.E., Yuen, H.F., O'Rourke, D., Babur, M., Telfer, B.A., Thomas, H.D., Keane, P., Nambirajan, T., et al. (2015). Vasoactivity of rucaparib, a PARP-1 inhibitor, is a complex process that involves myosin light chain kinase, P2 receptors, and PARP itself. *PLoS One* **10**, e0118187. <https://doi.org/10.1371/journal.pone.0118187>.
35. Ianevski, A., Giri, A.K., and Aittokallio, T. (2022). SynergyFinder 3.0: an interactive analysis and consensus interpretation of multi-drug synergies across multiple samples. *Nucleic Acids Res.* **50**, W739–W743. <https://doi.org/10.1093/nar/gkac382>.
36. Aubele, D.L., Hom, R.K., Adler, M., Galemno, R.A., Jr., Bowers, S., Truong, A.P., Pan, H., Beroza, P., Neitz, R.J., Yao, N., et al. (2013). Selective and brain-permeable polo-like kinase-2 (Plk-2) inhibitors that

- reduce alpha-synuclein phosphorylation in rat brain. *ChemMedChem* 8, 1295–1313. <https://doi.org/10.1002/cmcd.201300166>.
37. Zhang, C., Ni, C., and Lu, H. (2022). Polo-like kinase 2: from principle to practice. *Front. Oncol.* 12, 956225. <https://doi.org/10.3389/fonc.2022.956225>.
 38. Duda, P., Wiśniewski, J., Wójtowicz, T., Wójcicka, O., Jaśkiewicz, M., Drulis-Fajdasz, D., Rakus, D., McCubrey, J.A., and Gizak, A. (2018). Targeting GSK3 signaling as a potential therapy of neurodegenerative diseases and aging. *Expert Opin. Ther. Targets* 22, 833–848. <https://doi.org/10.1080/14728222.2018.1526925>.
 39. Sánchez-Danés, A., Richaud-Patin, Y., Carballo-Carbajal, I., Jiménez-Delgado, S., Caig, C., Mora, S., Di Guglielmo, C., Ezquerro, M., Patel, B., Giralt, A., et al. (2012). Disease-specific phenotypes in dopamine neurons from human iPSC-based models of genetic and sporadic Parkinson's disease. *EMBO Mol. Med.* 4, 380–395. <https://doi.org/10.1002/emmm.201200215>.
 40. di Domenico, A., Carola, G., Calatayud, C., Pons-Espinal, M., Muñoz, J.P., Richaud-Patin, Y., Fernandez-Carasa, I., Gut, M., Faella, A., Parameswaran, J., et al. (2019). Patient-specific iPSC-derived astrocytes contribute to non-cell-autonomous neurodegeneration in Parkinson's disease. *Stem Cell Rep.* 12, 213–229. <https://doi.org/10.1016/j.stemcr.2018.12.011>.
 41. Lill, C.M. (2016). Genetics of Parkinson's disease. *Mol. Cell. Probes* 30, 386–396. <https://doi.org/10.1016/j.mcp.2016.11.001>.
 42. Cai, R., Zhang, Y., Simmering, J.E., Schultz, J.L., Li, Y., Fernandez-Carasa, I., Consiglio, A., Raya, A., Polgreen, P.M., Narayanan, N.S., et al. (2019). Enhancing glycolysis attenuates Parkinson's disease progression in models and clinical databases. *J. Clin. Invest.* 129, 4539–4549. <https://doi.org/10.1172/JCI129987>.
 43. Sánchez-Danés, A., Consiglio, A., Richaud, Y., Rodríguez-Pizà, I., Dehay, B., Edel, M., Bové, J., Memo, M., Vila, M., Raya, A., and Izpisua Belmonte, J.C. (2012). Efficient generation of A9 midbrain dopaminergic neurons by lentiviral delivery of LMX1A in human embryonic stem cells and induced pluripotent stem cells. *Hum. Gene Ther.* 23, 56–69. <https://doi.org/10.1089/hum.2011.054>.
 44. Antolin, A.A., Clarke, P.A., Collins, I., Workman, P., and Al-Lazikani, B. (2021). Evolution of kinase polypharmacology across HSP90 drug discovery. *Cell Chem. Biol.* 28, 1433–1445.e3. <https://doi.org/10.1016/j.chembiol.2021.05.004>.
 45. Künzel, S.R., Hoffmann, M., Weber, S., Künzel, K., Kämmerer, S., Günscht, M., Klapproth, E., Rausch, J.S.E., Sadek, M.S., Kolanowski, T., et al. (2021). Diminished PLK2 induces cardiac fibrosis and promotes atrial fibrillation. *Circ. Res.* 129, 804–820. <https://doi.org/10.1161/CIRCRESAHA.121.319425>.
 46. Matthew, E.M., Yen, T.J., Dicker, D.T., Dorsey, J.F., Yang, W., Navaraj, A., and El-Deiry, W.S. (2007). Replication stress, defective S-phase checkpoint and increased death in Plk2-deficient human cancer cells. *Cell Cycle* 6, 2571–2578. <https://doi.org/10.4161/cc.6.20.5079>.
 47. Smeby, J., Kryeziu, K., Berg, K.C.G., Eilertsen, I.A., Eide, P.W., Johannessen, B., Guren, M.G., Nesbakken, A., Bruun, J., Lothe, R.A., and Sveen, A. (2020). Molecular correlates of sensitivity to PARP inhibition beyond homologous recombination deficiency in pre-clinical models of colorectal cancer point to wild-type TP53 activity. *EBioMedicine* 59, 102923. <https://doi.org/10.1016/j.ebiom.2020.102923>.
 48. Rao, A., Morris, D., Assikis, V.J., Jha, G.G., Ryan, C.J., Ablaza, A.-J., Habeck, J., Loehr, A., Xiao, J., and Gangolli, E.A. (2021). Rucaparib plus enzalutamide in patients (pts) with metastatic castration-resistant prostate cancer (mCRPC): Pharmacokinetics (PK) and safety data from the phase Ib RAMP study. *J. Clin. Oncol.* 39, 79. https://doi.org/10.1200/JCO.2021.39.6_suppl.79.
 49. Olsen, A.L., and Feany, M.B. (2019). PARP Inhibitors and Parkinson's Disease. *N. Engl. J. Med.* 380, 492–494. <https://doi.org/10.1056/NEJMcibr1814680>.
 50. Hu, Y., and Bajorath, J. (2014). Monitoring drug promiscuity over time. *F1000Res.* 3, 218. <https://doi.org/10.12688/f1000research.5250.2>.
 51. Zhou, J., Jiang, X., He, S., Jiang, H., Feng, F., Liu, W., Qu, W., and Sun, H. (2019). Rational Design of Multitarget-Directed Ligands: Strategies and Emerging Paradigms. *J. Med. Chem.* 62, 8881–8914. <https://doi.org/10.1021/acs.jmedchem.9b00017>.
 52. Melchiorre, C., Andrisano, V., Bolognesi, M.L., Budriesi, R., Cavalli, A., Cavrini, V., Rosini, M., Tumiatti, V., and Recanatini, M. (1998). Acetylcholinesterase noncovalent inhibitors based on a polyamine backbone for potential use against Alzheimer's disease. *J. Med. Chem.* 41, 4186–4189. <https://doi.org/10.1021/jm9810452>.
 53. Bolognesi, M.L., and Cavalli, A. (2016). Multitarget Drug Discovery and Polypharmacology. *ChemMedChem* 11, 1190–1192. <https://doi.org/10.1002/cmcd.201600161>.
 54. Cavalli, A., Bolognesi, M.L., Minarini, A., Rosini, M., Tumiatti, V., Recanatini, M., and Melchiorre, C. (2008). Multi-target-directed ligands to combat neurodegenerative diseases. *J. Med. Chem.* 51, 347–372. <https://doi.org/10.1021/jm7009364>.
 55. Antolin, A.A., Workman, P., Mestres, J., and Al-Lazikani, B. (2016). Polypharmacology in Precision Oncology: Current Applications and Future Prospects. *Curr. Pharmaceut. Des.* 22, 6935–6945. <https://doi.org/10.2174/1381612822666160923115828>.
 56. Lillich, F.F., Imig, J.D., and Proschak, E. (2020). Multi-Target Approaches in Metabolic Syndrome. *Front. Pharmacol.* 11, 554961. <https://doi.org/10.3389/fphar.2020.554961>.
 57. Hu, X., Zhang, J., Zhang, Y., Jiao, F., Wang, J., Chen, H., Ouyang, L., and Wang, Y. (2022). Dual-target inhibitors of poly (ADP-ribose) polymerase-1 for cancer therapy: Advances, challenges, and opportunities. *Eur. J. Med. Chem.* 230, 114094. <https://doi.org/10.1016/j.ejmech.2021.114094>.
 58. Li, X., Li, X., Liu, F., Li, S., and Shi, D. (2021). Rational Multitargeted Drug Design Strategy from the Perspective of a Medicinal Chemist. *J. Med. Chem.* 64, 10581–10605. <https://doi.org/10.1021/acs.jmedchem.1c00683>.
 59. Bottegoni, G., Favia, A.D., Recanatini, M., and Cavalli, A. (2012). The role of fragment-based and computational methods in polypharmacology. *Drug Discov. Today* 17, 23–34. <https://doi.org/10.1016/j.drudis.2011.08.002>.
 60. Zhang, N., Tian, Y.N., Zhou, L.N., Li, M.Z., Chen, H.D., Song, S.S., Huan, X.J., Bao, X.B., Zhang, A., Miao, Z.H., and He, J.X. (2021). Glycogen synthase kinase 3beta inhibition synergizes with PARP inhibitors through the induction of homologous recombination deficiency in colorectal cancer. *Cell Death Dis.* 12, 183. <https://doi.org/10.1038/s41419-021-03475-4>.
 61. Gaulton, A., Hersey, A., Nowotka, M., Bento, A.P., Chambers, J., Mendez, D., Motow, P., Atkinson, F., Bellis, L.J., Cibrián-Uhalte, E., et al. (2017). The ChEMBL database in 2017. *Nucleic Acids Res.* 45, D945–D954. <https://doi.org/10.1093/nar/gkw1074>.
 62. Antolin, A.A., Sanfelice, D., Crisp, A., Villasclaras Fernandez, E., Mica, I.L., Chen, Y., Collins, I., Edwards, A., Müller, S., Al-Lazikani, B., and Workman, P. (2023). The Chemical Probes Portal: an expert review-based public resource to empower chemical probe assessment, selection and use. *Nucleic Acids Res.* 51, D1492–D1502. <https://doi.org/10.1093/nar/gkac909>.
 63. Bertrand, J.A., Thieffine, S., Vulpetti, A., Cristiani, C., Valsasina, B., Knapp, S., Kalisz, H.M., and Flocco, M. (2003). Structural characterization of the GSK-3beta active site using selective and non-selective ATP-mimetic inhibitors. *J. Mol. Biol.* 333, 393–407. <https://doi.org/10.1016/j.jmb.2003.08.031>.
 64. Eid, S., Turk, S., Volkamer, A., Rippmann, F., and Fulle, S. (2017). KinMap: a web-based tool for interactive navigation through human kinome data. *BMC Bioinf.* 18, 16. <https://doi.org/10.1186/s12859-016-1433-7>.
 65. di Micco, P., Antolin, A.A., Mitsopoulos, C., Villasclaras-Fernandez, E., Sanfelice, D., Dolcianni, D., Ramagiri, P., Mica, I.L., Tym, J.E., Gingrich, P.W., et al. (2023). canSAR: update to the cancer translational research and drug discovery knowledgebase. *Nucleic Acids Res.* 51, D1212–D1219. <https://doi.org/10.1093/nar/gkac1004>.

66. Berman, H.M., Westbrook, J., Feng, Z., Gilliland, G., Bhat, T.N., Weissig, H., Shindyalov, I.N., and Bourne, P.E. (2000). The Protein Data Bank. *Nucleic Acids Res.* 28, 235–242. <https://doi.org/10.1093/nar/28.1.235>.
67. Anastasiadis, T., Deacon, S.W., Devarajan, K., Ma, H., and Peterson, J.R. (2011). Comprehensive assay of kinase catalytic activity reveals features of kinase inhibitor selectivity. *Nat. Biotechnol.* 29, 1039–1045. <https://doi.org/10.1038/nbt.2017>.
68. Ma, H., Deacon, S., and Horiuchi, K. (2008). The challenge of selecting protein kinase assays for lead discovery optimization. *Expert Opin. Drug Discov.* 3, 607–621. <https://doi.org/10.1517/17460441.3.6.607>.

STAR★METHODS

KEY RESOURCES TABLE

REAGENT or RESOURCE	SOURCE	IDENTIFIER
Chemicals, peptides, and recombinant proteins		
Rucaparib	Selleckchem	Cat#S4948
M324	Synthesized as part of this article.	
2-bromo-8-fluoro-4,5-dihydro-1H-azepino [5,4,3-cd]indol-6(3H)-one	Fluorochem	Cat#331126
4-boronobenzoic acid	Fluorochem	Cat#010786
3-(4,5-dimethylthiazol-2-yl)-2,5-diphenyltetrazolium bromide (MTT)	Sigma-Aldrich	Cat#M2128-1G
Puromycin dihydrochloride	Sigma-Aldrich	Cat#P7255-25MG
Sodium dodecyl sulfate solution	Sigma-Aldrich	Cat#05030-1L-F
Critical commercial assays		
HotSpot kinase screening platform	Reaction Biology	https://www.reactionbiology.com/assay-protocol-hotspot/
NanoBRET intracellular target engagement assays	Reaction Biology	https://www.reactionbiology.com/services/kinase-assays/nanobret-intracellular-kinase-assay/
Deposited data		
Database of chemical and pharmacological data curated from the medicinal chemistry literature	Gaulton et al. ⁶¹	https://doi.org/10.6019/CHEMBL.database.30
Dataset of rucaparib's major metabolite M324 concentration-response curves and IC50s values across the isolated kinases PLK2, GSK3A and GSK3B using biochemical assays.	This study canSAR knowledgebase	N/A
Database of chemical probes	Antolin et al. ⁶²	https://www.chemicalprobes.org/browse-probes
PLK2 structure co-crystalized with an inhibitor	Aubele et al. ³⁶	PDB: 4I5M
GSK3B structure co-crystalized with an inhibitor	Bertrand et al. ⁶³	PDB: 1Q3W
Experimental models: Cell lines		
HEK293 cells (female, human embryonic kidney)	ATCC	CRL-1573™
Software and algorithms		
CLARITY	Vidal et al. ²⁶	https://www.chemotargets.com
SEA	Lounkine et al. ²⁷	https://sea.bkslab.org/
PPB2	Awale et al. ²⁸	https://ppb2.gdb.tools/
GalaxySagittarius	Yang et al. ²⁹	http://galaxy.seoklab.org/sagittarius
KinMap	Eid et al. ⁶⁴	http://www.kinhub.org/kinmap/#
ADMETlab 2.0	Xiong et al. ³⁰	https://admetmesh.scbdd.com/
GraphPad Prism version 9.0	GraphPad Software Inc., San Diego, CA, USA	https://www.graphpad.com/scientific-software/prism/
MOE 2020.09	Vilar et al. ³¹	https://www.chemcomp.com/Products.htm
SynergyFinder 3.0	Ianevski et al. ³⁵	https://synergyfinder.fimm.fi

RESOURCE AVAILABILITY

Lead contact

Further information and requests for resources and reagents should be directed to and will be fulfilled by the lead contact, Albert A. Antolin (Albert.Antolin@icr.ac.uk).

Materials availability

This study only generated M324 as a new reagent, that can be easily synthesized using the method described below. We have a small quantity of M324 left that is available upon request.

Data and code availability

- The published article includes all datasets generated during this study and publicly available as the date of publication. These datasets are also freely available in the public canSAR knowledgebase and can be accessed from the “Resources” section, under “Other resources” (<https://cansar.ai/resources/>).⁶⁵ This article also analyzed data from the publicly available resources ChEMBL⁶¹ (<https://www.ebi.ac.uk/chembl/>) and PDB⁶⁶ (<https://www.rcsb.org/>) using external software (see [key resources table](#) for details).
- This paper does not report original code.
- Any additional information required to reanalyze the data reported in this paper is available from the [lead contact](#) upon request.

EXPERIMENTAL MODEL AND STUDY PARTICIPANT DETAILS

Cell lines

HEK293 cells (female, human), which were established from primary embryonic human kidney, were obtained from ATCC and tested free of mycoplasma upon arrival using the MycoAlert Mycoplasma Detection Kit (Lonza, cat# LT07-118). This cell line was not authenticated in our hands, all experiments with this cell line were performed at the Contract Research Organization Reaction Biology. The cells were transfected using EMEM +10% FBS +1% P/S medium. The assay itself was performed in Opti-MEM I reduced serum medium, without phenol red. EMEM was purchased from ATCC and Opti-MEM was purchased from ThermoFisher. The rest of cell lines were originally obtained from ATCC, authenticated, and mycoplasma was tested by standard PCR methods every month.

METHOD DETAILS

Procedure for the preparation of metabolite M324

To a solution of 2-bromo-8-fluoro-4,5-dihydro-1H-azepino[5,4,3-*cd*]indol-6(3H)-one (0.16 g, 0.57 mmol) in a mixture of toluene (15 mL) and ethanol (7.5 mL), sodium carbonate (0.15 g, 1.43 mmol), 4-boronobenzoic acid (0.14 g, 0.86 mmol) and water (0.4 mL) were added sequentially. The solution was degassed with argon and Pd(Ph₃P)₄ (33 mg, 0.03 mmol) was added. The mixture was heated at reflux for 5 h. Then, the solution was cooled to room temperature and diluted with water (20 mL). The aqueous layer was adjusted to pH 7–8 with HCl 1N and a solid was formed. The precipitate was filtered rendering 130 mg (71%) of desired compound.

Kinase off-target predictions using four different computational methods

In this analysis, we used four different *in silico* approaches covering various algorithms, namely: (1) the commercial target prediction software CLARITY from Chemotargets (<https://www.chemotargets.com>) which incorporates six independent ligand-based methods (e.g., machine learning, simplest active subgraph, etc) which were used in a consensus manner to perform the comparison of chemical structures between compounds of interest and bioactive compounds with known binding targets;²⁶ (2) the public similarity ensemble approach (SEA) (<https://sea.bkslab.org/>), which derives macromolecule predictions based on the chemical similarity scores between the ligands;²⁷ (3) the public polypharmacology browser PPB2 (<https://ppb2.gdb.tools/>), which features different models (e.g., fingerprint comparison, machine learning or deep learning) to predict potential targets based on bioactivity data from ChEMBL.²⁸ We used the two best performing models from PPB2: (a) nearest neighbor (NN) similarity searching with the multinomial Naive Bayes machine learning model (NB) using the ECFP4 fingerprint (**NN(ECfp4) + NB(ECfp4)**), and (b) integrating NN using shape and pharmacophore fingerprint (Xfp) with NB model of the ECFP4 fingerprint (**NN(Xfp) + NB(ECfp4)**); the predictions from both approaches were concatenated to yield the final prediction results; and (4) GalaxySagittarius (<http://galaxy.seoklab.org/sagittarius>) uses ligand similarity comparison to prefilter large-volume data prior to a time-consuming docking procedure.²⁹ From the target prediction outputs of GalaxySagittarius, we selected the top 100 targets based on ranked docking scores as our results. For all four approaches, in line with our hypothesis, we only selected the targets that were human protein kinases as the final output of each method. [Tables S1–S4](#) list the predictions obtained from these four computational methods.

In vitro kinome profiling using biochemical assays on isolated proteins and concentration-response curves

M324 was profiled against a kinome panel comprising 370 human kinases employing the HotSpot technology from Reaction Biology (<http://www.reactionbiology.com>)⁶⁷ at 10 μM concentration ([Figure 4A](#); [Table S5](#)). Kinases more potently inhibited by M324 were

further tested at 1 μ M (Table S6, n = 2) and/or 10-point concentration-response (Table S9, n = 3). The employed *in vitro* kinase radiometric assay directly measures phosphorylation of substrate via consuming 33 P-labelled ATP to obtain the kinase catalytic activity. Radioisotope-labelled proteins and peptides in the HotSpot assay are captured via spotting of the reaction mix on a filter membrane, whereas unreacted phosphate is washed away from the filter papers.⁶⁸

In vitro PARP family profiling using biochemical assays on isolated proteins

All PARP family profiling assays were performed following the BPS PARP or TNKS assay kit protocols (<https://bpsbioscience.com/research-areas/poly-adt-ribose-polymerase/assay-kits>). The enzymatic reactions were conducted in duplicate at room temperature for 1 h in a 96 well plate coated with histone substrate. 50 μ L of reaction buffer (Tris·HCl, pH 8.0) contained NAD⁺, biotinylated NAD⁺, activated DNA, a PARP enzyme and the test compound. After enzymatic reactions, 50 μ L of Streptavidin-horseradish peroxidase was added to each well and the plate was incubated at room temperature for an additional 30 min. Next, 100 μ L of developer reagents were added to wells and luminescence was measured using a BioTek SynergyTM 2 microplate reader. PARP or TNKS activity assays were performed in duplicate. The luminescence data were analyzed using the computer software Graphpad Prism. In the absence of the compound, the luminescence (Lt) in each dataset was defined as 100% activity. In the absence of the PARP or TNKS, the luminescence (Lb) in each dataset was defined as 0% activity. The percent activity in the presence of each compound was calculated according to the following equation: % activity = [(L - Lb)/(Lt - Lb)] \times 100, where L = the luminescence in the presence of the compound, Lb = the luminescence in the absence of the PARP or TNKS, and Lt = the luminescence in the absence of the compound. The percent inhibition was calculated according to the following equation: % inhibition = 100 - % activity. Tables S7 and S8 list the results of the experimental PARP profiling of M324 and its comparison with rucaparib.

Intracellular target engagement kinase assays

We used Reaction Biology's NanoBRET platform (<http://www.reactionbiology.com>) that uses biophysical approaches to determine the kinase inhibitor occupancy of a ligand in intact living cells using BRET and an optimized cell-permeable kinase tracer. The specificity of the BRET signal is dictated by the placement of NanoLuc on the specific kinase and transfected into HEK293 cells, which were established from primary embryonic human kidney.

Human embryonic kidney (HEK293) cells were purchased from ATCC. FuGENER HD Transfection Reagent, KinaseNanoLuc fusion plasmids, Transfection Carrier DNA, NanoBRET Tracer and dilution buffer, NanoBRET Nano-Glo Substrate, Extracellular NanoLuc Inhibitor were from Promega. AT7519 and BI-2536 were used as positive controls for the determination cellular activities of GSK3A and PLK2, respectively.

HEK293 cells were transiently transfected with the KinaseNanoLuc Fusion Vector DNA using FuGENER HD Transfection Reagent. Test compounds were dispensed into 384 well assay plate using an Echo 550 acoustic dispenser (Labcyte Inc, Sunnyvale, CA). Transfected cells were harvested and mixed with NanoBRET Tracer Reagent and dispensed into 384 well plates and incubated at 37 $^{\circ}$ C in 5% CO₂ cell culture incubator for 1 h. The NanoBRET Nano-Glo Substrate plus Extracellular NanoLuc Inhibitor Solution were added into the wells of the assay plate and incubated for 2–3 min at room temperature. The donor emission wavelength (460 nm) and acceptor emission wavelength (600 nm) were measured in an EnVision plate reader. The BRET Ratio was calculated using the equation: BRET Ratio = [(Acceptor sample \div Donor sample) - (Acceptor no-tracer control \div Donor no-tracer control)]. Table S10 shows the raw data of this intracellular target engagement experiment.

Docking studies

To explore the molecular interactions of M324 and rucaparib with their stronger kinase hits we used the docking method available in MOE 2020.09 (<https://www.chemcomp.com/Products.htm>).³¹ From the three kinases more potently inhibited by M324 *in vitro*, only two – GSK3B and PLK2 – had a crystal structure deposited in the PDB and, therefore, are the focus of this study. We choose the X-ray complex with the closest molecular size or most similar scaffold to rucaparib to increase the accuracy of the modeling: (1) the crystallographic structure of PLK2 in complex with BI 2536 (PDB ID: 4I5M),³⁶ an ATP-competitive inhibitor, was used to predict the interactions of rucaparib and M324 on PLK2 kinase; (2) the X-ray complex co-crystallized with alsterpaullone (PDB ID: 1Q3W),⁶³ which contains an amide-bearing tetracyclic scaffold, was selected for GSK3B. Prior to the docking studies, crystal structures were corrected for missing atoms and bonds, and protonated under physiological condition using standard methods available in MOE. Water molecules were only removed provided the absence of water-mediated interactions in original structures. The co-crystallised ligands were exploited to define the active site and the general default parameters for docking were applied.

MTT cell viability assays

Cellular viability was evaluated using standard 3-(4,5-dimethylthiazol-2-yl)-2,5-diphenyltetrazolium bromide (MTT)-based assays (Sigma-Aldrich) as performed in previous works.^{32,33} For each cell line, cells were seeded in 96-well plates to reach confluence (90%) at the end of the experiment (96 h). Table S11 lists the number of cells per well and media used for each of the twenty cancer cell lines that we screened. Cells were supplemented the next day (24 h) with control compound (puromycin dihydrochloride, Sigma-Aldrich), rucaparib (Selleckchem), M324 or a combination of M324 and rucaparib at different concentrations. After 96 h, cells were treated for 3 h with 10 μ L per well of MTT solution (5 mg/mL MTT (Sigma-Aldrich) in water), a yellow tetrazole that is reduced to purple formazan crystals by living cells. Formazan crystals were dissolved with 100 μ L of solubilization buffer (10% SDS (Sigma-Aldrich) and

10 mM HCl (Panreac) in water) overnight. Plates were read at optical density = 560 nm in a spectrophotometer, and then the percentage of viable cells compared to the untreated wells was determined (Tables S11 and S12).

Cell culture experiments with human iPSC lines and M324 treatment

The competent Spanish authorities (Commission on Guarantees concerning the Donation and Use of Human Tissues and Cells of the Carlos III National Institute of Health) approved the use of human iPSCs in this work. The iPSC lines used in our studies were previously generated and fully characterized.^{39,40} Specifically, we used one iPSC line obtained from a healthy donor (SP11, control) and one iPSC line obtained from PD patients carrying the LRRK2 G2019S mutation (SP12, LRRK2-PD). Directed differentiation toward midbrain dopaminergic neurons (DAn) was carried out using a 30-day protocol based on DAn patterning factors and co-culture with mouse PA6 feeding cells to provide trophic factor support, with minor modifications.^{42,43} Specifically, iPSCs were cultured in mTeSR commercial medium until they reached 80% confluence and then mechanically aggregated to form embryoid bodies (EBs) in 96-well plate, without using lentiviral vectors to express LMX1A transcriptional factor. EBs were cultured for 10 days in suspension in N2B27 medium, consisting of DMEM/F12 medium (GIBCO), neurobasal medium (GIBCO), 0.5 × B27 supplement (GIBCO), 0.5 × N₂ supplement (GIBCO), 2 mM ultraglutamine (Lonza) and penicillin-streptomycin (Lonza). In this differentiation step, N2B27 was supplemented with SHH (100 ng/mL, Peprotech), FGF-8 (100 ng/mL, Peprotech), and bFGF (10 ng/mL, Peprotech). Neuronal progenitor cells (NPCs) were then co-cultured with PA6 stromal cells for 3 weeks in N2B27 medium, as described.^{40,41} Finally, for α -synuclein analysis, neuronal cultures were gently trypsinized and re-plated on Matrigel-coated slides. Two days after plating, midbrain DAn were treated for 24 h with 20 μ M M324, after which cells were fixed and analyzed.

Immunofluorescence analyses of iPSC-derived DA neurons

DA neurons were fixed with 4% paraformaldehyde (PFA, ref. 19210, Anamed), blocked and permeabilized with TBS with low Triton (0.01% Triton X-100) and 3% donkey serum for 2 h. Subsequently, cells were incubated for 48 h at 4°C with the following primary antibodies: rabbit anti-TH (1:1000, T8700, Sigma), and mouse anti- α -syn (1:500, 610787, BD Biosciences). Samples were then incubated with secondary antibodies for 2 h at RT: Cy3 anti-rabbit IgG (1:200, 711-165-152, Jackson ImmunoResearch), and Alexa Fluor 488 anti-mouse IgG (1:200, 715-545-150, Jackson ImmunoResearch). To visualize nuclei, slides were stained with DAPI (1:5000, Invitrogen) and then mounted with PVA:DABCO. Images were then acquired using a LSM880 ZEISS confocal microscope and analyzed with FIJI Is Just ImageJ. The scoring of α -syn-positive DAn was performed by researchers blinded to the experimental conditions.

QUANTIFICATION AND STATISTICAL ANALYSIS

IC₅₀, EC₅₀ and hill slope determination

The IC₅₀ and EC₅₀ values (concentration causing a half-maximal inhibition of control specific activity) and Hill coefficients (nH) were determined by non-linear regression analysis of the inhibition curves generated with mean replicate values using Hill equation curve-fitting ($Y = D + [(A - D)/(1 + (C/C_{50})^{nH})]$, where Y = specific activity, D = minimum specific activity, A = maximum specific activity, C = compound concentration, C₅₀ = IC₅₀, and nH = slope factor). This analysis was performed using the GraphPad Prism version 9.0 (GraphPad Software Inc., San Diego, CA, USA) (<https://www.graphpad.com/scientific-software/prism/>). In Figure 5, n represents the number of replicates, and all the statistical details can be found in the Figure legends and the raw data in the Table S9 and S10. Statistical analyses of the obtained data in Figure 7 were performed using ANOVA, and were plotted using Prism version 9.00 for Mac (GraphPad Software, La Jolla, CA, USA) with SEM error bars. ***p < 0.001, **p < 0.01.

Synergy analysis

The expected effect of a drug combination can be estimated mathematically, using a reference or null model, which quantifies the expected combination effect under the null hypothesis of no interaction between the single agents.³⁵ We used SynergyFinder web-application version 3.0 (<https://synergyfinder.fimm.fi>), which enables simultaneous analysis and interactive visualization of drug combinations assessed with multiple synergy reference models.³⁵ We analyzed LNCaP and DU145 independent experiments 1 (Table S12) using SynergyFinder 3.0, corrected outliers, and used the recommended LL4 model for curve fitting. Synergy scores and maps were calculated with several models including Bliss, Loewe, ZIP and HAS.³⁵